2013

Uncertainty quantification of film cooling effectiveness in gas turbines

Hessam Babaee
Louisiana State University and Agricultural and Mechanical College, hbabae1@lsu.edu

UNCERTAINTY QUANTIFICATION OF FILM COOLING EFFECTIVENESS IN GAS TURBINES

A Thesis

Submitted to the Graduate Faculty of the
Louisiana State University and
Agricultural and Mechanical College
in partial fulfillment of the
requirements for the degree of
Master of Science

in

The Department of Mathematics

by
Hessam Babaee
M.Sc., University of Tehran, 2006
August 2013

Acknowledgments

I would like to thank my adviser Dr. Xiaoliang Wan for many hours of insightful conversations we had that helped me learn a lot about high-order methods. I also would like to thank Professor Sumanta Acharya, my PhD adviser in Mechanical Engineering, for his constant encouragement and support throughout this research.

This research was supported by a grant from AFOSR and a grant from the DEPSCoR-AFOSR programs. This support is gratefully acknowledged. The simulations were performed on Louisiana Optical Network Initiative (LONI) systems and High Performance Computing systems at Louisiana State University.

My parents Ahmad and Mahin have been behind me in all my endeavors. Without their unconditional love and support this thesis would not be the same.

Table of Contents

List of Tables

List of Figures

Abstract

In this study the effect of uncertainty of velocity ratio on jet in crossflow and particularly film cooling performance is studied. Direct numerical simulations have been combined with a stochastic collocation approach where the parametric space is discretized using Multi-Element general Polynomial Chaos (ME-gPC) method. Velocity ratio serves as a bifurcation parameter in a jet in a crossflow and the dynamical system is shown to have several bifurcations. As a result of the bifurcations, the target functional is observed to have low-regularity with respect to the paramteric space. In that sense, ME-gPC is particularly effective in discretizing the parametric space. One particular case of a jet in a crossflow is numerically solved with the velocity ratio variations assumed to have a truncated Gaussian distribution with mean of 1.5 and the standard variation of approximately 0.5. Five elements are used to discretize the parametric space using ME-gPC method. Within each element general polynomial chaos of order 3 is used. A fast convergence of the polynomial expansion in the parametric space was observed. Time-dependent Navier-Stokes equations are sampled at Gauss-quadrature points using spectral/hp element method implemented in $\mathcal{N}\epsilon\kappa\mathcal{T}\alpha r$. Overall due to the low-regularity of the response surface, ME-gPC is observed to be a computationally effective strategy to study the effect of uncertainty in a jet in a crossflow when velocity ratio is the random parameter.

Chapter 1
Introduction

Gas turbines ideally operate based on Brayton cycle. In this thermodynamic cycle input air is pressurized in an isentropic process by passing through compressor. In the second process, high-pressure air enters the combustion chamber where the ignition of the fuel increases the energy level of the working fluid in a constant-pressure process. The flow has its highest amount of energy content and temperature upon leaving the combustion chamber. Next, the high-pressure and high-temperature gas enters a multi-stage turbine in which its energy is extracted by turbine in an isentropic process. The energy extracted by the turbine is used to drive the compressor shaft and in the case of land-based gas turbines the turbine also provides energy to rotate the generator shaft. In the case of a jet engine, the working fluid exits the gas turbine with high momentum. The difference between the momentum of the working fluid in the exit and inlet of the engine provides the thrust for the aircraft.

1.1 Film cooling

Since gas turbines operate based on Brayton cycle, increasing the turbine inlet temperature directly increases the thermal efficiency of the thermodynamic cycle [15]. However the temperature of the inlet gas is limited by the melting point of the turbine blade metal. To allow higher inlet gas temperatures, three main strategies are commonly employed: (1) *Thermal Barrier Coating (TBC)* in which a ceramic layer covers the blade metal surface and protects it from exposure to hot gas; (2) *internal cooling* where the coolant extracts heat by moving through the internal passages inside the blade and (3) *film cooling* in which the coolant flow is extracted from the the compressor and is bled through discrete film holes on the surface of the blade. The role of the coolant layer is to protect the components on the hot gas path and therefore increases the life of these components.

Film cooling is currently a widely used technology in modern gas turbines. The objective in designing an efficient film cooling strategy is to achieve maximum cooling perfor-

mance by using the least amount of coolant possible while ensuring high degree of confidence in the *durability* of the gas turbine.

1.1.1 Uncertainty quantification in film cooling

The design parameters in film cooling can vary significantly from their desired values due to inherent uncertainties in engine operating conditions. The resulting variations can unfavorably affect the film cooling performance which in turn severely impact the durability of the components that have exposure to hot gases. An increase of $25°C$ in the temperature of these components can reduce their life time by a factor of two [9], and given that the turbine inlet temperatures are in the range of $1400°C - 1600°C$, a high degree of sensitivity exits between an increase of temperature of the hot gas components and their durability.

One of the most important control parameters in designing a film cooling strategy is the *blowing ratio (BR)*, defined as $BR = \rho_j V_j / \rho_\infty V_\infty$ where the subscript j and ∞ denote jet and crossflow respectively and ρ is density and V is velocity. In cases where $\rho_j = \rho_\infty$, the blowing ratio becomes equivalent to the *velocity ratio* (R) defined as $R = V_j / V_\infty$. In cases with low blowing ratio, insignificant amount of coolant in injected which rapidly mixes out with the hot gas and results in poor coverage of the surface. On the other hand, at high blowing ratios the coolant separates from the surface, allowing the hot gas penetration behind the jet which increases the surface temperature. Thus, intuitively an optimal blowing ratio exits that corresponds to a maximum film cooling effectiveness. However blowing ratio is not a deterministic value at engine operating conditions, as shown by Abhari [1] for instance, who reported $\pm 100\%$ around the design blowing ratio due to the rotor-stator interaction. From the point of view of designing a turbine cooling system, it is important to obtain a quantitative tool with which the effect of uncertainty of design parameters on the temperature of hot gas components can be investigated. The main objective of the current thesis, is to study the effect of uncertainty of blowing ratio on film cooling effectiveness.

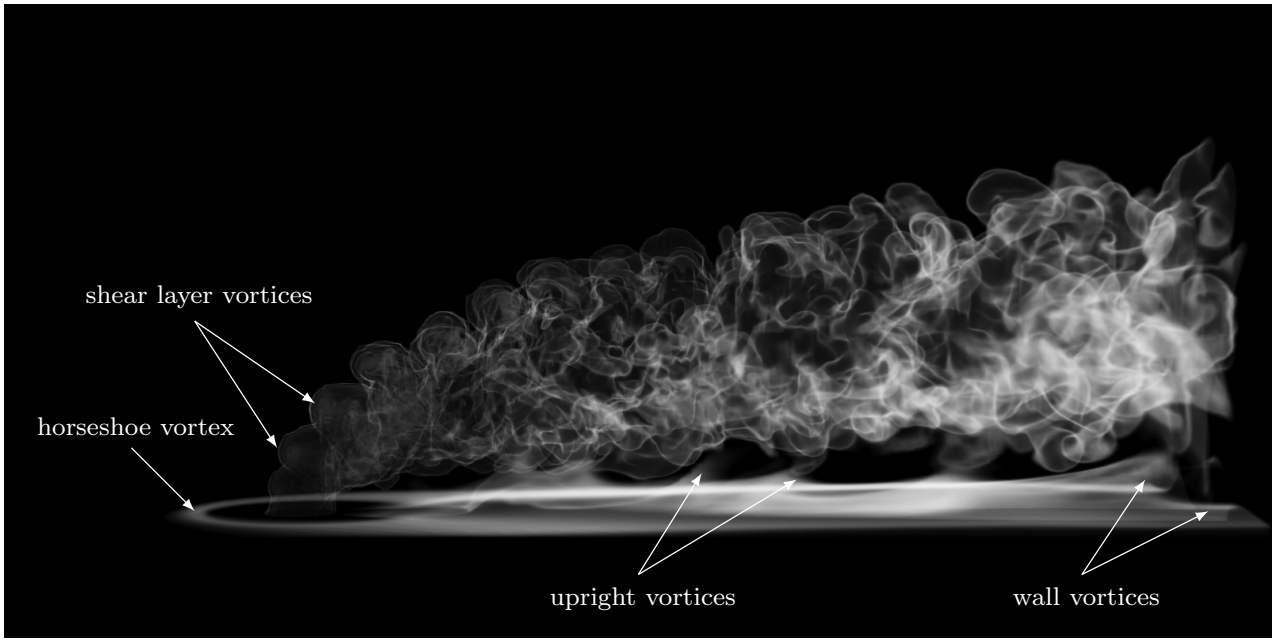

Figure 1.1: Smoke visualization of the scalar field at velocity ratio $R = 2$. The details of the computation are given in [4], chapter 2.

1.2 Flow dynamics of film cooling

Film cooling problem is studied as a *jet in a crossflow (JICF)* where the coolant (jet) is flushed into the hot gas (crossflow). A large body of experimental ([12, 21, 36, 8]) and numerical ([47, 29, 34, 26]) studies have investigated the dynamics of the JICF. In general five vortical structures dominate the dynamics of JICF as shown in figure 1.1 shown in figure (only four of them are shown): (1) *Counter-rotating Vortex Pair (CVP)* visible in time-averaged plots; (2) *shear layer vortices*; (3) *horseshoe vortex*; (4) *upright vortices*; and (5) *wall vortices*. For more description on the above vortex structures see [4], chapter 1.

1.2.1 Bifurcation in the dynamical system

The connection between the study of dynamical systems and turbulence was first made by Hopf [16] and then by Landau and Lifshitz [23]. They suggested a road map for a series of transitions from steady to periodic and then quasi-periodic attractors as the bifurcation parameter (Reynolds number) increases. In this analogy, flow corresponds to a phase flow on an n-dimensional torus in state space of the dynamical system.

Recently Ilak *et al.* [17] performed a bifurcation analysis for a vertical jet in a crossflow.

They consider the velocity ratio R as the bifurcation parameter. They found three critical values of R at which the corresponding dynamical system of the Navier-Stokes equations undergoes a transition. Their study was the continuation of the global stability analysis carried out by Bagheri [6], who found that three instability mechanisms coexist at velocity ratio $R = 3$. These instability mechanisms along with their corresponding velocity ratios are shown in table 1.1, which is re-produced here from Ilak *et al.* [17]. In their numerical investigation using linear stability analysis, Ilak *et al.* [17] showed that for $R < 0.675$ the flow is steady. However as velocity ratio increases to values above $R \simeq 0.675$, self-sustained oscillations emerge. These oscillations appear in the form of hairpin vortices that are periodically shed downstream of the jet with a sharp peak frequency in the energy spectrum. Transition from a steady solution to a limit cycle suggests that Hopf bifurcation occurs as the velocity ratio increases above the the critical value of $R \simeq 0.675$. The linear stability analysis carried out by Bagheri [6] shows that this transition is the result of growth of instabilities in the shear layer and is of Kelvin-Helmholtz type (see table 1.1).

As the value of R further increases, two other instability mechanisms occur which have been documented by Bagheri [6] and Ilak *et al.* [17]. These two mechanisms and their corresponding velocity ratios are presented in table 1.1.

Bifurcation in the dynamical system such as a JICF can potentially play an important role in the investigating the propagation of randomness throughout such systems, especially when the bifurcation parameter is the random parameter/process whose impact is being investigated, since often the dynamical systems that undergo a bifurcation, show an abrupt change in their response. This can be particularly important when spectral methods such as polynomial chaos are used to investigate the effect of uncertainty of the bifurcation parameter on the response of the dynamical system, since the bifurcation can directly affect the regularity of the *response surface* as a function of the bifurcation parameter. Low-regularity of the response surface adversely affects the convergence rate of the spectral method.

Table 1.1: Instability mechanisms in vertical jet in crossflow as bifurcation parameter R varies. The table is re-produced and slightly modified from Ilak *et al.*[17] Table 1.

Local mechanism	Symmetry	Location	R
Kelvin-Helmholtz instability	Symmetric	Jet region	$R > 0.675$
Elliptic instability	Antisymmetric	Jet and wake region	$R > 2.25$
von-Kármán instability	Antisymmetric	Wall region	$R > 2.5$

In the current study, the randomness of velocity ratio, which is an important design parameter in film cooling application, is investigated and as demonstrated the velocity ratio is a bifurcation parameter in a JICF. The focus of the current thesis is to present a numerically efficient method for investigating uncertainty in such systems.

1.3 Numerical simulations for film cooling

One of the main considerations in studying the effect of uncertainty in film cooling applications is the computational cost of solving such a problem. Film cooling problem has been extensively studied both numerically and experimentally. The majority of the numerical simulations have utilized Reynolds Averaged Navier-Stokes (RANS) equations which rely on turbulence models. These models have been shown to be unsuitable to accurately capture the dynamics of the flow and high-fidelity numerical simulations that resolve the relevant spatial and temporal scales in the flow are required [3]. Large Eddy Simulation (LES) has been shown to be a reliable tool in solving film cooling problems [2, 32, 18, 14, 33] by resolving the large scale structures and modeling the smaller scales. Nevertheless using any turbulence model brings a new source of uncertainty to the problem that unless it is quantified, can interfere with the randomness imposed by the boundary condition such as velocity ratio. Direct Numerical Simulation (DNS), on the other hand, resolves all relevant time and space scales without using a model and it has been successfully used to simulate turbulent flows in film cooling [5, 25].

1.4 Numerical methods for solving stochastic partial differential equations

As a numerical strategy in stochastic computations, Monte Carlo methods and its variants are of the most widely used approaches. This family of methods require sampling of the deterministic system at random inputs. Monte Carlo methods are especially attractive when a large number of random variables are considered, since their convergence rates do not depend or weakly depend on the number of random dimensions. However, Monte Carlo methods are prohibitively expensive for our problem, where each sample requires solving an expensive Direct Numerical Simulation (DNS) with several millions degree of freedom.

In cases with only a few random variables, spectral methods in which the target function is represented as an expansion of fast-converging polynomials, can be far more efficient, especially when the functional relationship between the random variable and the target function is smooth. The spectral methods are relatively new in the field of stochastic computation and they have enjoyed a rapid growth in the last decade in the numerical simulation of random/stochastic partial differential equations [45]. The first variant of these approaches is the Polynomial Chaos (PC) where the Hermite polynomials constitute an orthogonal expansion basis of the probability space. The coefficients of the expansion are obtained by employing a Galerkin projection. This method was pioneered by Ghanem and Spanos [13] for solving stochastic differential equations and was extended by Xiu and Karniadakis [46] to general Polynomial Chaos (gPC) which includes a broader family of polynomials from the Asky scheme. The gPC method was successfully used to solve Navier-Stokes equations with random inflows [37]. In cases where sufficient smoothness between the input random variable and the target random function does not exist, increasing polynomial order can be inefficient [39]. To remedy this limitation, Wan and Karniadakis [38] developed a multi-element extension (ME-gPC) to the general polynomial chaos, in which the random space is first decomposed into a number of finite elements. Within each element an orthogonal polynomial expansion is employed; this is a concept analogous to the spectral element approach that has been used for the deterministic problems.

In chapter 2 of the current thesis, a detailed review and investigation of the spectral methods used to investigate uncertainty in systems governed by partial differential equations is given.

1.5 Objective and Outline

The goal of the current study is to investigate the effect of the uncertainty in the velocity ratio on a jet in a crossflow. We present a computationally efficient strategy to investigate the effect of randomness in velocity ratio on the performance of film cooling. We combine DNS using spectral/hp finite element method and ME-gPC method as a strategy to discretize the parametric space.

In chapter 2, a detailed review of the spectral methods for solving stochastic partial differential equations is presented. In chapter 3, the mathematical model that governs the jet in a crossflow is given. Also the details of numerical method including discretization in physical and parametric spaces are presented. In chapter 4, the explained numerical methods are then applied to a three-dimensional jet-in-crossflow problem. The summary is given in chapter 5.

The outcome of the study enables us to quantify the effect of randomness in velocity ratio on a jet in a crossflow and particularly on the surface temperature or cooling effectiveness. To the best knowledge of the author, this is the first study that investigates jet in a crossflow in a probabilistic framework.

Chapter 2
Spectral methods

2.1 Probabilistic framework

The mathematical framework that is considered in this thesis is limited to stochastic systems that are a system of partial/ordinary differential equations and random inputs are introduced at boundary/initial conditions. Since the objective of the current study is to investigate the effect of uncertainty in film cooling applications, which are governed by Navier-Stokes and energy equations (*i.e.* a system of partial differential equations) and randomness is most commonly introduced to the system as random boundary conditions, the choice of current framework is justified.

Let $(\Omega, \mathcal{F}, \mathcal{P})$ be a complete probability space, where Ω is the sample space, $\mathcal{F}$ is the σ-algebra of all subsets of Ω and $\mathcal{P}$ is the probability measure. The expectation of the random process is correspondingly given by:

$$\mathbb{E}[X(t,\omega)] = \int_{\Omega} X(t,\omega) d\mathcal{P}.$$

We consider the random input to be a random process $X(t,\omega)$ where

$$X(t,\omega) : [0,T] \times \Omega \longrightarrow \mathbb{R}, \qquad T \in \mathbb{R}^{+}. \tag{2.1}$$

We also assume that $X(t,\omega)$ is a second-order random process *i.e.* $X(t,\omega) \in L_2(\Omega, \mathcal{F}, \mathcal{P})$. The space of $L_2(\Omega, \mathcal{F}, \mathcal{P})$ is defined by all random processes for which: $\mathbb{E}[X(t,\omega)^2] < \infty$.

2.2 Karhunen–Loève decomposition

To parametrize $X(t,\omega)$, the procedure of Karhunen–Loève (K-L) decomposition is commonly employed to efficiently reduce the dimensionality of the random process. Let the covariance for the random process given by equation 2.1 be:

$$K(t,s) = \mathbb{E}[X(t,\omega)X(s,\omega)], \qquad \forall (t,s) \in [0,T] \times [0,T]. \tag{2.2}$$

The random process can now be represented as:

$$X(t,\omega) = \sum_{i=1}^{\infty} \sqrt{\lambda_i}\psi_i(t)\xi_i(\omega), \tag{2.3}$$

where $\{\lambda_i, \psi_i\}_{i=1}^{\infty}$ are eigenvalue-eigenfunctions of the autocorrelation kernel:

$$\int_0^T K(t,s)\psi_i(s)ds = \lambda_i\psi_i(t), \qquad t \in [0,T], \quad i = 1,2,\ldots. \tag{2.4}$$

The eigenfunctions ψ_i's are mutually orthogonal and the random variables ξ_i's are uncorrelated:

$$\int_0^T \psi_i(t)\psi_j(t)dt = \delta_{ij} \qquad i,j = 1,2,\ldots, \tag{2.5}$$

and

$$\mathbb{E}[\xi_i\xi_j] = \delta_{ij} \qquad i,j = 1,2,\ldots. \tag{2.6}$$

The dimension reduction of the random process is performed by truncating the spectral expansion given by equation 2.3. This follows:

$$X_d(t,\omega) = \sum_{i=1}^{d} \sqrt{\lambda_i}\psi_i(t)\xi_i(\omega). \tag{2.7}$$

The error of this expansion is given by:

$$\epsilon_d = \int_0^T \mathbb{E}[X(t,\omega) - X_d(t,\omega)]^2 dt = \sum_{i=d+1}^{\infty} \lambda_i. \tag{2.8}$$

The efficiency of the dimension reduction using K-L decomposition depends on the regularity and correlation length of the kernel $K(t,s)$. For a fixed correlation length, lower regularity of $K(t,s)$ reduces the convergence rate of the K-L decomposition or equivalently increases the number of dimensions required to reach a certain level of accuracy. On the other hand, for a fixed kernel, larger correlation length increases the convergence rate of

the K-L decomposition, or equivalently reduces the number of dimensions for a given level of accuracy.

As an example we consider a Gaussian and an exponential kernel defined as:

$$K_G(t,s) = \exp(-A(t-s)^2/l_c^2), \qquad \forall (t,s) \in [0,T] \times [0,T], \tag{2.9}$$

and

$$K_E(t,s) = \exp(-A|t-s|/l_c), \qquad \forall (t,s) \in [0,T] \times [0,T], \tag{2.10}$$

where $K_G(t,s)$ and $K_E(t,s)$ denote Gaussian and exponential kernels respectively, A is the normalization constant and l_c is the correlation length. The value of A has chosen to be $A = 6$ to give a direct physical meaning to the correlation length, *i.e* the correlation becomes nearly zero at $|t-s| = l_c$. This choice of parameter was used in [37].

In figure 2.1 few selected eigenfunctions ($\{\psi_i\}$'s) of Gaussian kernel with correlation length of $l_c = 4$ are shown. These eigenfunctions provide an efficient orthogonal basis for the Gaussian kernel. In figure 2.2 the correlation functions of the Gaussian and exponential kernels are shown. The correlation function of exponential kernel is smaller than that of the Gaussian kernel due to the low-regularity of the exponential kernel.

The energy captured by the d-term expansion of the K-L decomposition is:

$$\mathcal{E}_d = \sum_{i=1}^{d} \lambda_i, \tag{2.11}$$

and the total energy is

$$\mathcal{E} = \sum_{i=1}^{\infty} \lambda_i. \tag{2.12}$$

Thus the relative energy captured by a truncated K-L decomposition is given by:

$$\mathcal{E}_d/\mathcal{E} = \frac{\sum_{i=1}^{d} \lambda_i}{\sum_{i=1}^{\infty} \lambda_i}. \tag{2.13}$$

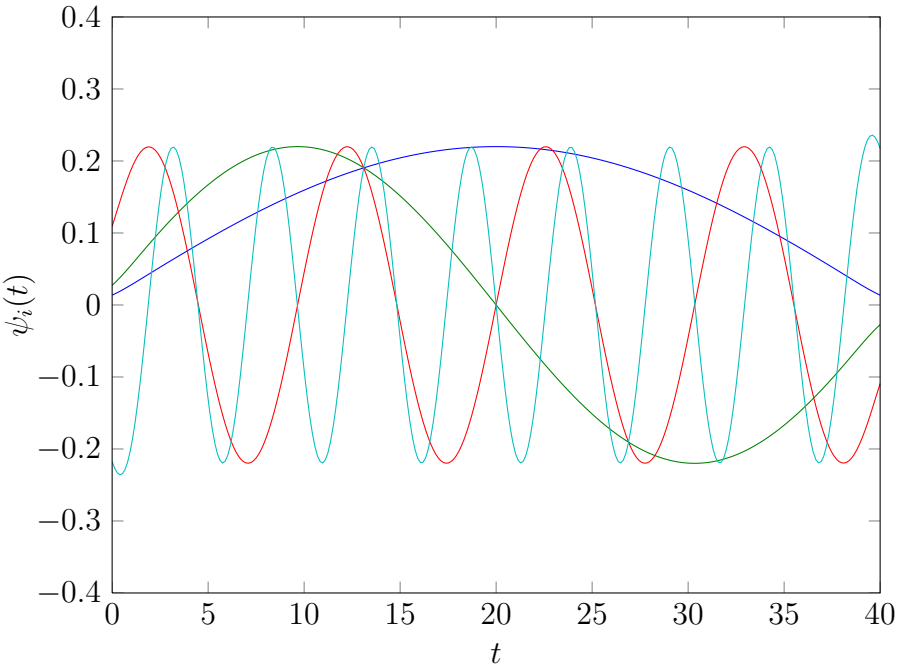

Figure 2.1: Selected eigenfunctions for the Gaussian kernel $K_G(t,s)$ with correlation length of $l_c = 4$.

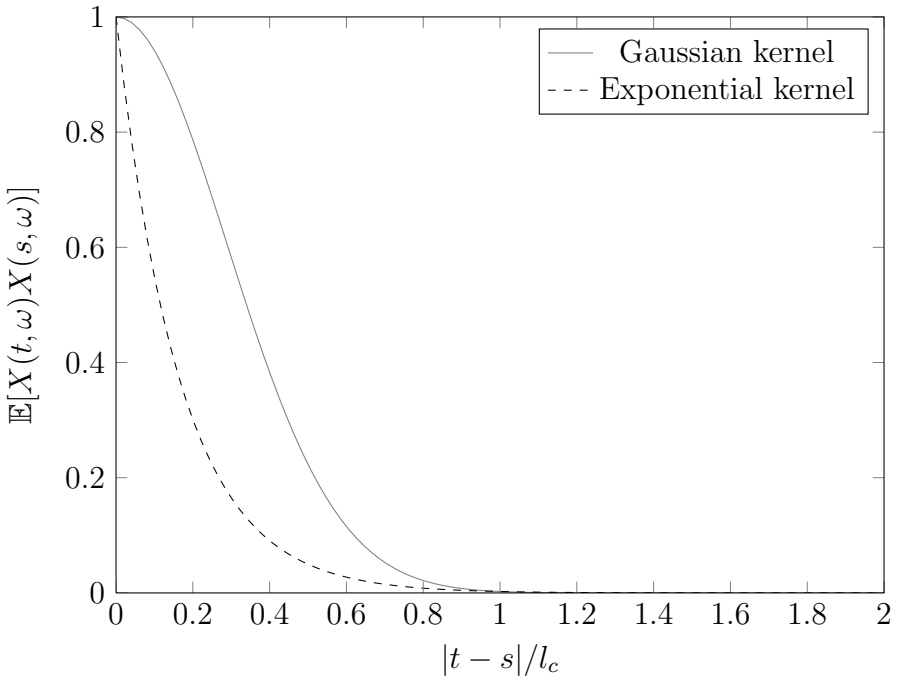

Figure 2.2: Correlation functions for Gaussian $K_G(t,s)$ and exponential $K_E(t,s)$ kernels.

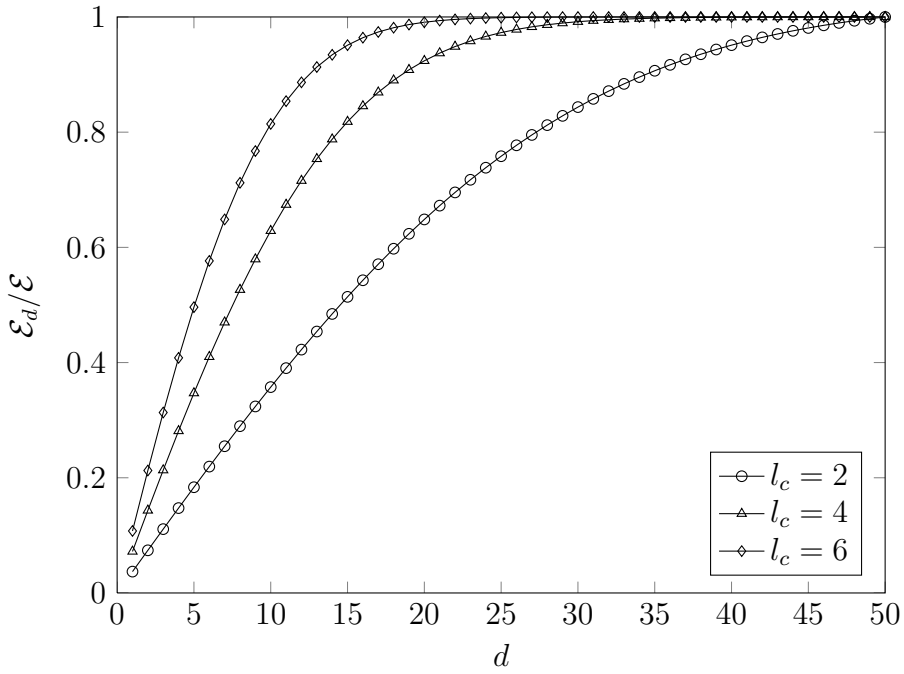

Figure 2.3: Relative energy captured by Karhunen–Loève decomposition of Gaussian kernel $K_G(t, s)$ for different correlation lengths.

In figure 2.3, the relative energy of a fixed Gaussian kernel captured by K-L decomposition is compared for different correlation lengths. It is clear that the kernels with smaller correlation length require a larger number of expansion terms to capture a desired level of relative energy.

Figure 2.4(a) and 2.4(b) show the random processes sampled from Gaussian kernels with correlation lengths of $l_c = 2$ and $l_c = 8$. Intuitively the Gaussian kernel with smaller correlation length ($l_c = 2$) shows "high frequency" variations whereas the kernel with $l_c = 8$ shows "lower frequency" variations when compared to those observations of random processes with smaller correlation length. As mentioned earlier in this section, the low-regularity of the correlation kernel results in the slower decay of the spectral decomposition as given by equation 2.3. Figure 2.5 shows the comparison between the spectral decay of the Gaussian and exponential kernels with the same correlation length of $l_c = 4$. Due to the low-regularity of the exponential kernel, the decay rate of its spectral decomposition is smaller than that of the Gaussian kernel, which is a smooth kernel.

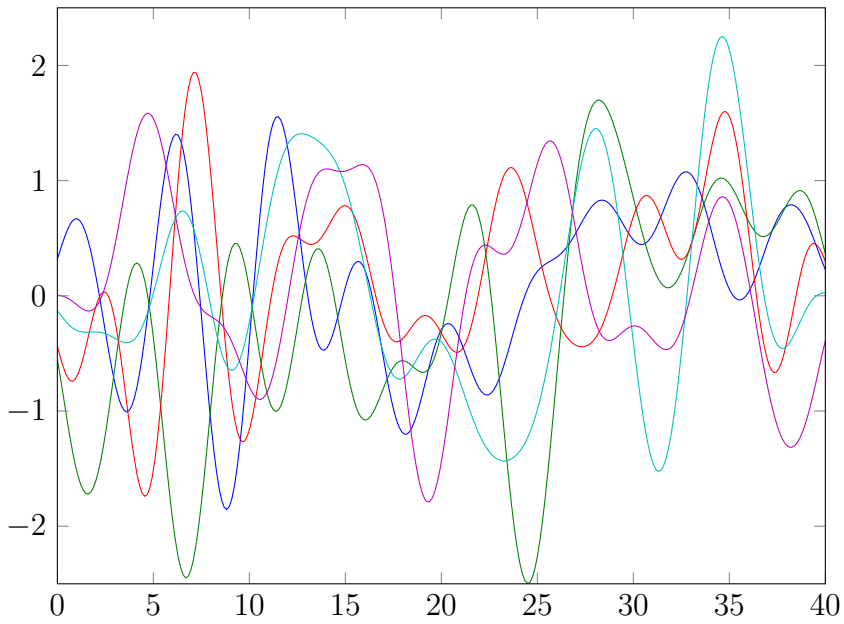

(a) $l_c = 2$

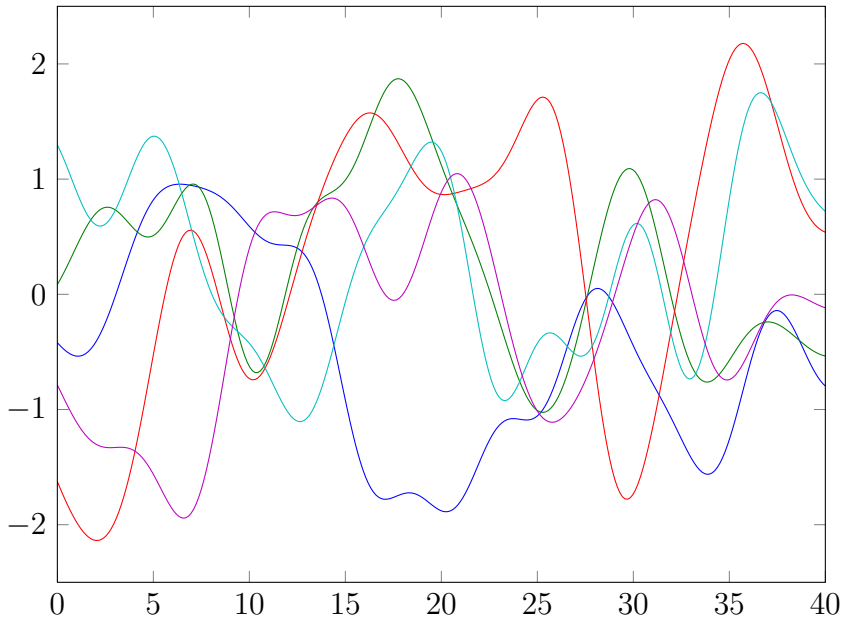

(b) $l_c = 8$

Figure 2.4: Sample observations of random processes with Gaussian kernel: (a) correlation length $l_c = 2$; (b) correlation length $l_c = 8$.

2.3 Notation of the reduced-order random process

By performing the dimension reduction as explained in the previous section, we can formulate the finite-dimensional random system.

Let $\boldsymbol{\xi} = (\xi_1(\omega), \ldots, \xi_d(\omega))$ be an d-variate random vector with independent components

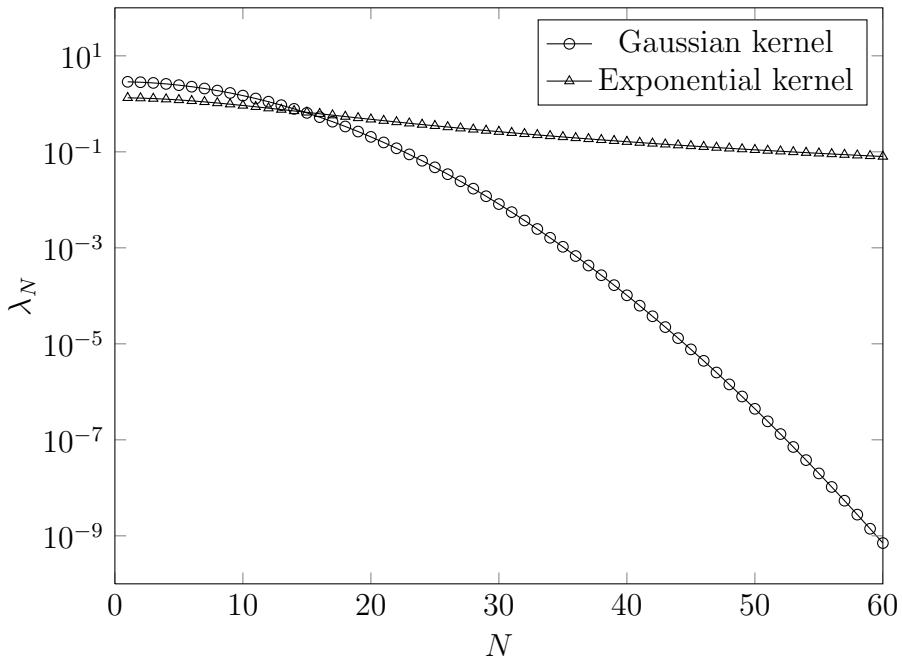

Figure 2.5: Comparisons of spectral decay of Gaussian and exponential kernels with the same correlation length of $l_c = 4$.

in the probability space defined above, where d is the number of dimensions in the random space after performing dimension reduction. Let $\mu_i : \Gamma_i \longrightarrow \mathbb{R}^+$ be the probability density function (PDF) of the random variable $\xi_i(\omega)$, $\omega \in \Omega$ with the range of $\Gamma_i \triangleq \xi_i(\Omega) \subset \mathbb{R}$. Since the random variables ξ_i's are independent (assuming Gaussian random processes), the joint PDF of the random vector $\boldsymbol{\xi} = (\xi_1(\omega), \ldots, \xi_d(\omega))$ is the multiplication of the PDF of each of the random components. This follows:

$$\mu(\boldsymbol{\xi}) = \prod_{i=1}^{d} \mu_i(\xi_i), \tag{2.14}$$

with the support of μ being:

$$\Gamma \triangleq \prod_{i=1}^{d} \Gamma_i \subset \mathbb{R}^d. \tag{2.15}$$

2.4 Polynomial chaos

Polynomial chaos, also known as *homogeneous chaos*, was first introduced by Wiener in 1938 to study the theory of turbulence [42]; a proposition that was discarded by Orszag and Bissonnette [30] roughly thirty years later. In 1947, Cameron and Martin [10] used

Hermite polynomials as a complete orthonormal basis to represent a second-order random process in a Fourier expansion.

Let C denote the space of continous real functions on the interval $0 \leq t \leq 1$ which vanish at $t = 0$, and W_t be the Wiener process. Also let the set of multi-indices with finite number of non-zero elements be:

$$\mathcal{J} = \{\boldsymbol{i} = (i_1, i_2, \dots) | i_j \in \{0, 1, 2, \dots\}, j \in \mathbb{N}, |\boldsymbol{i}| = \sum_{j=1}^{\infty} i_j < \infty\}. \tag{2.16}$$

Let $\{\alpha_i(t)\}_{i=1}^{\infty}$ be an orthonormal set in $L_2(0, 1)$. According to Paley and Wiener [31], $\xi_i(\omega) = \int_0^1 \alpha_i(t) dW_t$ is a Gaussian random number with mean zero and variance of $\int_0^1 \alpha_i(t)^2 dt = 1$. Also note that ξ_i's are uncorrelated:

$$\mathbb{E}[\xi_i \xi_j] = \delta_{ij}, \tag{2.17}$$

where δ_{ij} is the Kronecker delta. For the verification of the above equation see for instance [22]. Therefore ξ_i's are independent standard Gaussian random numbers.

Now we introduce the basis functional:

$$\boldsymbol{\phi_i}(\boldsymbol{\xi}(\omega)) = \prod_{j=1}^{\infty} H_{i_j}(\xi_j(\omega)), \tag{2.18}$$

where $H_{i_j}(\xi_j(\omega))$ are Hermite polynomials of order i_j, and $\boldsymbol{\xi}(\omega) = \{\xi_1(\omega), \xi_2(\omega), \dots\}$.

We now present the Fourier-Hermite expansion for a second-order random process (Cameron-Martin theorem):

Theorem 1 *If $Y(\omega)$ is a functional of $L_2(C)$,* i.e. *$\mathbb{E}[Y(\omega)^2] < \infty$, then the Fourier-Hermite expansion*

$$Y(\omega) = \sum_{|\boldsymbol{i}|=0}^{\infty} a_{\boldsymbol{i}} \boldsymbol{\phi_i}(\boldsymbol{\xi}(\omega)) \tag{2.19}$$

where $a_{\boldsymbol{i}} = \mathbb{E}[Y(\omega)\boldsymbol{\phi_i}(\boldsymbol{\xi}(\omega))]$ converges in $L_2(C)$ sense.

2.5 General polynomial chaos

Polynomial chaos has been successfully used to model Gaussian random inputs in solid mechanics, however a general framework is required to solve stochastic differential equations with non-Gaussian processes as input. Recently Xiu and Karniadakis [46] extended the idea of polynomial chaos to specific random variables whose Probability Density Function (PDF) has correspondence to the weight of orthogonal polynomials of *Asky* family.

To demonstrate the efficiency of gPC approximation we intentionally use Hermite-chaos polynomials to approximate $f(x(\omega))$ where $x(\omega)$ is a random number with Gamma distribution given by:

$$\rho(x) = \exp(-x), x > 0$$

Thus we consider:

$$f(x(\omega)) = \sum_{i=0}^{N} a_i \phi_i(\xi(\omega)), \tag{2.20}$$

where $\xi(\omega)$ is a standard normal random number with the PDF of $\mu(\xi) = 1/\sqrt{2\pi}\exp(-\xi^2/2)$ and $\phi_i(\xi(\omega))$ are Hermite-chaos polynomials of degree i. Using Galerkin projection the Fourier coefficients can be found with:

$$a_i = \frac{(f(x), \phi(\xi))}{\|\phi_i(\xi)^2\|}, \tag{2.21}$$

where the inner product and its induced norm are defined with respect to the Gaussian weight $\mu(\xi)$:

$$(f, g) := \int_{\mathbb{R}} f(\xi) g(\xi) \mu(\xi) d\xi, \qquad \|f(\xi)\| := (f, f)^{1/2}. \tag{2.22}$$

Since in equation 2.21, x is a random variable with Gamma distribution, $f(x)$ has to be represented with respect to ξ. This issue can be resolved by transforming $x(\omega)$ to a uniform random number $u(\omega) \in \mathcal{U}(0, 1)$. Introducing the Cumulative Density Functions (CDF) for both $\xi(\omega)$ and $x(\omega)$ by:

$$F(x) = \int_0^x \rho(y) dy = 1 - \exp(-x) \tag{2.23}$$

and

$$G(\xi) = \int_{-\infty}^{\xi} \mu(y)dy \tag{2.24}$$

Therefore we have:

$$\begin{aligned} u(\omega) = F(x(\omega)), \quad &\longrightarrow \quad x(\omega) = F^{-1}(u(\omega)) \\ u(\omega) = G(\xi(\omega)), \quad &\longrightarrow \quad \xi(\omega) = G^{-1}(u(\omega)), \end{aligned} \tag{2.25}$$

Thus we have:

$$x(\omega) = F^{-1}(G(\xi(\omega))) \tag{2.26}$$

Using equations 2.23 and 2.26 we have:

$$x(\omega) = -\log(1 - G(\xi(\omega))) \tag{2.27}$$

Equation 2.27 is now used in the inner product in equation 2.21 to calculate the Fourier coefficients.

Figure 2.6 shows the Hermite-chaos expansion to approximate the random variable x with gamma distribution. Although this expansion is convergent, large oscillations are observed near $x = 0$. however note that a Lahuerre-chaos expansion with polynomial order one approximates x exactly which shows the efficiency of Lahuerre-chaos for approximating Gamma random functions. The similar numerical efficiency can be observed for random variables given in table 2.1 when an expansion of the polynomials that are orthogonal with respect to their PDFs are used.

2.6 Multi-Element general Polynomial Chaos

In this section we describe the ME-gPC approach to solve stochastic partial differential equations. More details about this section can be found at [38]. In the ME-gPC approach the parametric space is decomposed to non-overlapping elements and that is the main difference between gPC and ME-gPC. Thus in ME-gPC approach h-refinement can be

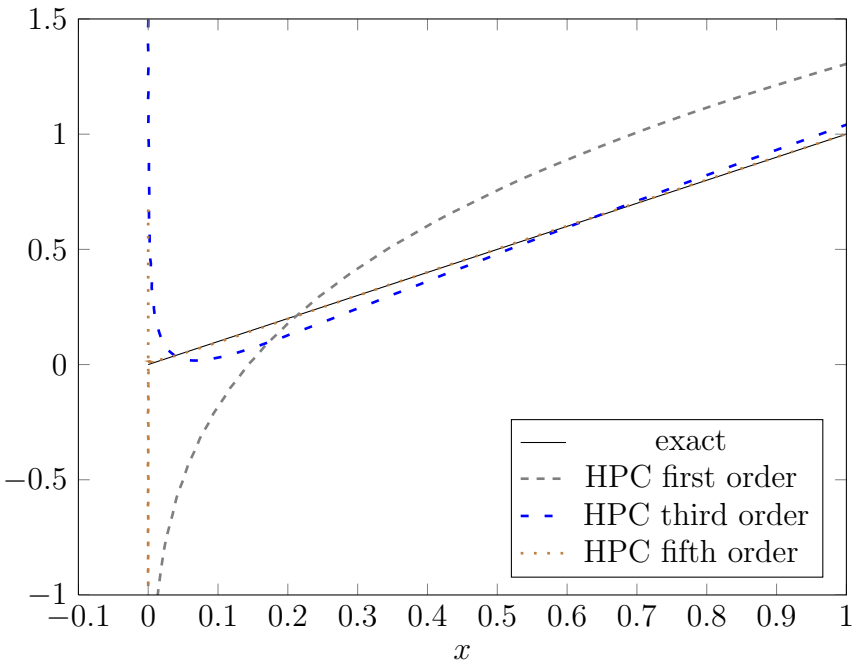

Figure 2.6: Approximation of random variable x with gamma distribution by Hermite-chaos expansion.

performed when the response function does not have sufficient regularity.

Table 2.1: Wiener-Askey polynomials and their underlying polynomials

	Random variables $\boldsymbol{\xi}$	Wiener-Askey chaos $\{\phi_\alpha(\boldsymbol{\xi})\}$	Support
Continuous	Gaussian	Hermite-chaos	$(-\infty, \infty)$
	gamma	Lahuerre-chaos	$[0, \infty)$
	beta	Jacobi-chaos	$[a, b]$
	uniform	Legendre-chaos	$[a, b]$
Discrete	Poisson	Charlier-chaos	$\{0, 1, 2, \dots\}$
	binomial	Krawtchouk-chaos	$\{0, 1, 2, \dots, N\}$
	negative binomial	Meixner-chaos	$\{0, 1, 2, \dots\}$
	hypergeometric	Hahn-chaos	$\{0, 1, 2, \dots, N\}$

2.6.1 Decomposition in parametric space

In ME-gPC strategy, the parametric space is decomposed to non-overlapping elements as follows:

$$\mathbf{D} = \begin{cases} B_e = [a_{e,1}, b_{e,1}) \times [a_{e,2}, b_{e,2}) \times \cdots \times [a_{e,d}, b_{e,d}) \quad e = 1, 2, \ldots, Ne, \\ B = \bigcup_{e=1}^{Ne} B_e, \\ B_{e1} \bigcap B_{e2} = \emptyset \quad \text{if } e_1 \neq e_2, \quad e_1, e_2 = 1, 2, \ldots, Ne, \end{cases} \tag{2.28}$$

where B_e is an element in the parametric space and $a_{e,i}$ and $b_{e,i}$ are the beginning and the end of element B_e in i^{th} direction respectively, and Ne is the number of elements. We introduce the indicator random variable:

$$I_{B_e}(\boldsymbol{\xi}) = \begin{cases} 1, & \boldsymbol{\xi} \in B_e, \\ 0, & \text{otherwise.} \end{cases} \tag{2.29}$$

From the law of total probability we have:

$$Pr(\boldsymbol{\xi} \leq \boldsymbol{q}) = \sum_{e=1}^{Ne} Pr(\boldsymbol{\xi} \leq \boldsymbol{q} \mid I_{B_e} = 1) Pr(I_{B_e} = 1), \tag{2.30}$$

where $\boldsymbol{q} \in \mathbb{R}^d$ is an arbitrary point, $Pr(\mathcal{E})$ is the probability of event $\mathcal{E}$, and $Pr(\mathcal{E} \mid \mathcal{F})$ is the conditional probability and represents the probability of event $\mathcal{E}$ given that event $\mathcal{F}$ has occurred. Also note that from the definition of the indicator random variable given by equation 2.29, we arrive at:

$$Pr(I_{B_e} = 1) = \int_{B_e} \mu(\boldsymbol{\xi}) d\boldsymbol{\xi},$$

and since $\int_B \mu(\boldsymbol{\xi})\boldsymbol{\xi} = 1$, we have:

$$\sum_{e=1}^{Ne} Pr(I_{B_e} = 1) = 1.$$

Moreover the set of $\{I_{B_e}^{-1}(1)|e = 1, 2, \ldots, Ne\}$ constitutes a non-overlapping decomposition of sample space Ω, *i.e.*:

$$\Omega = \bigcup_{e=1}^{Ne} I_{B_e}^{-1}(1)$$

Now we can define a local random variable $\hat{\boldsymbol{\xi}}$ in each element as

$$\hat{\boldsymbol{\xi}}^e = (\hat{\xi_1}^e, \hat{\xi_2}^e, \ldots, \hat{\xi_d}^e) : I_{B_e}^{-1} \mapsto B_e.$$

The probability density function of $\hat{\boldsymbol{\xi}}$ is obtained using Bayes' rule:

$$\hat{\mu}_e(\hat{\boldsymbol{\xi}}^e) := \mu(\boldsymbol{\xi} \mid I_{B_e} = 1) = \frac{\mu(\boldsymbol{\xi})}{Pr(I_{B_e} = 1)}, \tag{2.31}$$

where $\mu(\boldsymbol{\xi} \mid I_{B_e} = 1)$ is the conditional PDF with the condition of $I_{B_e} = 1$.

The expectation of a generic function $f(\boldsymbol{\xi})$ in the global domain B is obtained by:

$$\mathbb{E}(f(\boldsymbol{\xi})) = \int_B f(\boldsymbol{\xi})\mu(\boldsymbol{\xi})d\boldsymbol{\xi}. \tag{2.32}$$

The local expectation in each element B_e is obtained by:

$$\mathbb{E}_e[f(\hat{\boldsymbol{\xi}}^e)] = \int_{B_e} f(\hat{\boldsymbol{\xi}}^e)\hat{\mu}_e(\hat{\boldsymbol{\xi}}^e)d\hat{\boldsymbol{\xi}}^e. \tag{2.33}$$

Using equations 2.30, 2.32 and 2.33, we reach at:

$$\mathbb{E}[f(\boldsymbol{\xi})] = \sum_{e=1}^{Ne} Pr(I_{B_e} = 1)\mathbb{E}_e[f(\hat{\boldsymbol{\xi}}^e)]. \tag{2.34}$$

Equation 2.34 provides a basis for the calculation of statistical information from the elemental to the global level.

2.6.2 Discretization of parametric space

In this section an efficient polynomial basis to discretize the parametric space is described. We carry out the discretization in one dimension for simlicity. The extension to higher dimensions is straightforward and is achieved using tensor product of one-dimensional basis.

We assume that $f(\xi(\omega))$ is a second-order random variable, *i.e.* $f(\xi(\omega)) \in L_2(\Omega, \mathcal{F}, \mathcal{P})$. Let $\mathcal{P}_M(f)$ denote the Galerkin projection of $f(\xi)$ onto polynomial chaos basis of $\{\phi(\xi)\}_i$ up to polynomial order M. From the theorem by Cameron and Martin [10] we know that:

$$\mathbb{E}[(f(\xi) - \mathcal{P}_M f(\xi))^2] \to 0 \qquad \text{as} \quad M \to \infty. \tag{2.35}$$

According to proposition 2.1 in [38] it is easy to show that from global convergence given by equation 2.35 that the local convergence at elemental level is followed:

$$\mathbb{E}_e[(f(\hat{\xi}^e) - \mathcal{P}_M f(\hat{\xi}^e))^2] \to 0 \qquad \text{as} \quad M \to \infty. \tag{2.36}$$

Since polynomials $\{\phi(\xi)\}_i$ are orthogonal, the error of the Galerkin projection, $f(\xi) - \mathcal{P}_M f(\xi)$ is orthogonal to $V(\xi; M) := \text{span}\{\phi(\xi) : i \leq M\}$. However error at local level, $f(\hat{\xi}^e) - \mathcal{P}_M f(\hat{\xi}^e)$ is not in general orthogonal to the space $V(\hat{\xi}^e; M)$ with respect to the conditional PDF $\hat{\mu}_e(\hat{\xi}^e)$. Orthogonality in the elemental level is key to the efficiency of ME-gPC method, since for a given elemental decomposition, orthogonal basis are efficient in the sense of being the optimal choice of polynomial basis that minimizes the projection error $\mathbb{E}[(f(\xi) - \mathcal{P}_M f(\xi))^2]$.

Wan and Karniadakis [38] proposed a numerical procedure to construct elemental polynomials that are orthogonal with respect to the conditional PDF $\hat{\mu}_e(\hat{\xi}^e)$. We denote such a basis with $\hat{V}(\xi; M, Ne) := \text{span}\{\phi_i^e(\xi) : \ i = 0, \ldots, M, \ e = 1, \ldots, Ne\}$ where $\phi_i^e(\xi)$ are local

polynomials of order i and e denotes the element number. A zero extension of polynomial $\phi_i^e(\xi)$ in region outside the element B_e is assumed, *i.e.*:

$$\phi_i^e(\xi) = 0, \qquad \xi \quad \notin B_e.$$

The polynomials $\phi_i^e(\xi)$ for $i = 0, \dots M$ are mutually orthogonal with respect to the local PDF of $\hat{\mu}_e(\xi)$. In other words:

$$\mathbb{E}_e[\phi_i^e(\xi)\phi_j^e(\xi)] = (\gamma_i^e)^2\delta_{ij}, \tag{2.37}$$

where γ_i^e is the local norm of the polynomial $\phi_i^e(\xi)$ and is given by:

$$\gamma_i^e = (\mathbb{E}_e[\phi_i^e(\xi)^2])^{1/2}. \tag{2.38}$$

Note that by considering the zero expansion of polynomial $\phi_i^e(\xi)$ outside of the element B_e, orthogonality in the global sense is also retained, *i.e.*:

$$\mathbb{E}[\phi_i^e(\xi)\phi_j^e(\xi)] = Pr(I_{B_e} = 1)(\gamma_i^e)^2\delta_{ij}. \tag{2.39}$$

Chapter 3
Uncertainty quantification for film cooling

In this chapter, the details of the numerical algorithm used to investigate the effect of uncertainty of boundary conditions on film cooling performance are presented. A typical schematic of flow interaction in film cooling application is shown in figure 3.1. The coolant is injected through small holes on the blade surface. The delivery tube, which is connected to a plenum (not shown in figure 3.1), is inclined to lower the likelihood of flow separation behind the coolant jet. In the next section the mathematical model that governs the flow physics of the film cooling application is presented.

3.1 Governing equations

We solve the incompressible Navier-Stokes equations for velocity and pressure along with the advection-diffusion equation for temperature. The assumptions made to reach at these equations are given in [4]. These equations in non-dimensional form are given by:

$$\nabla \cdot \mathbf{u} = 0, \tag{3.1}$$

$$\frac{\partial \mathbf{u}}{\partial t} + (\mathbf{u} \cdot \nabla)\mathbf{u} = -\nabla p + \frac{1}{Re}\nabla^2 \mathbf{u}, \tag{3.2}$$

$$\frac{\partial \theta}{\partial t} + (\mathbf{u} \cdot \nabla)\theta = \frac{1}{RePr}\nabla^2 \theta, \tag{3.3}$$

where $\mathbf{x} = \{x_1, x_2, x_3\}$ is the Cartesian coordinate, t is time, $\mathbf{u} = \mathbf{u}(\mathbf{x}, t; \boldsymbol{\xi})$, $p = p(\mathbf{x}, t; \boldsymbol{\xi})$ and $\theta = \theta(\mathbf{x}, t; \boldsymbol{\xi})$ are non-dimensional Cartesian velocity vector, pressure and temperature respectively and $\boldsymbol{\xi}$ is the random vector that is obtained by parametrization of the random boundary conditions. Prandtl number is denoted by Pr and Reynolds number by Re defined as $Re = u_{ref} l_{ref}/\nu$ with u_{ref} and l_{ref} as the characteristic velocity and length respectively. Temperature (T) is non-dimensionalized using

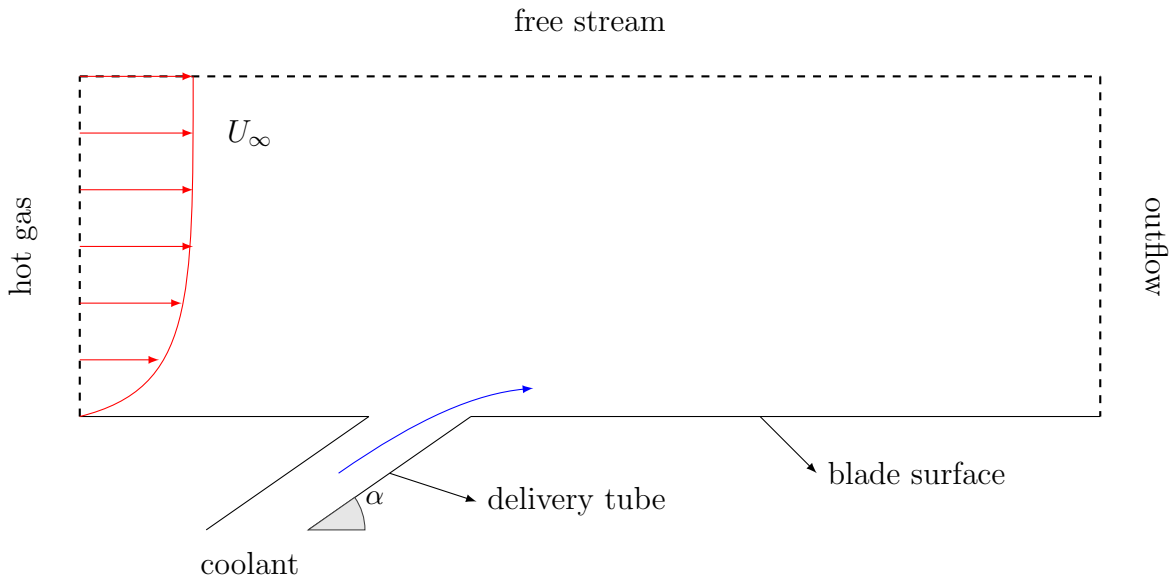

Figure 3.1: Two-dimensional schematic of a typical film cooling model.

$$\theta(\mathbf{x}, t; \boldsymbol{\xi}) = (T(\mathbf{x}, t; \boldsymbol{\xi}) - T_c)/(T_h - T_c),$$

where T_h is the hot gas temperature and T_c is the coolant temperature. The interaction between the coolant (jet) and the hot gas (crossflow) results in a complex three-dimensional flow which is often turbulent and contains a wide range of scales in time and space. Throughout this thesis, direct numerical simulation is performed to solve equations 3.1-3.3. Thus all relevant scales in time and space, from *integral* to *Kolmogorov* scales are numerically resolved. In the next three sections the main components of the numerical approach used in this thesis are presented.

3.2 Discretization in space: spectral/hp element

For discretization in space, we use spectral/hp element method implemented in $\mathcal{N}\epsilon\kappa\mathcal{T}\alpha r$ [41]. The spectral/hp method has the geometric flexibility of h-type finite element method, while it benefits from the fast convergence of spectral methods. These two characteristics of spectral/hp element method make it a particularly attractive method for the film cooling problem studied in the current research, where local h-refinement near the jet exit is required.

In this section the components of the spectral/hp element method are reviewed. For a more detailed explanation see [20].

For space discretization modal polynomials within each element are used as the basis. We use hexahedral elements throughout this research. The three-dimensional basis are obtained by the tensor product of the following one-dimensional basis [20]:

$$\phi_p(\xi) = \begin{cases} \dfrac{1-\xi}{2}, & p = 0, \\ (\dfrac{1-\xi}{2})(\dfrac{1+\xi}{2})P_{p-1}^{1,1}, & 0 < p < P, \\ \dfrac{1+\xi}{2}, & p = P, \end{cases} \tag{3.4}$$

where $P^{(\alpha,\beta)}$ are the Jacobi polynomials. The family of Jacobi polynomials are the solutions to a singular Sturm-Liouville problem in the region of $-1 < x < 1$:

$$\frac{d}{dx}\left[(1-x)^{(1+\alpha)}(1+x)^{(1+\beta)}\frac{d}{dx}P_p^{(\alpha,\beta)}(x)\right] = \lambda_p(1-x)^{\alpha}(1+x)^{\beta}P_p^{(\alpha,\beta)}(x), \tag{3.5}$$

where $\lambda_p = -p(\alpha+\beta+p+1)$. An interesting property of the Jacobi polynomials is their orthogonal relationship:

$$\left(P_p^{(\alpha,\beta)}(x), P_q^{(\alpha,\beta)}(x)\right)_w = C\delta_{pq}, \tag{3.6}$$

where δ_{pq} is Kronecker delta and $w(x)$ serves as the weight of the inner product in the following sense:

$$\left(f, g\right)_w := \int_{-1}^{1} f(x)g(x)w(x)dx, \qquad w(x) = (1-x)^{\alpha}(1+x)^{\beta}.$$

The one-dimensional basis 3.4 are shown in figure 3.2 for $P = 4$.

The expansion to three dimension is obtained by tensor product of one-dimensional basis:

$$u(\xi_1, \xi_2, \xi_3) = \sum_{r=0}^{P}\sum_{q=0}^{P}\sum_{p=0}^{P}\hat{u}_{pqr}\phi_p(\xi_1)\phi_q(\xi_2)\phi_r(\xi_3). \tag{3.7}$$

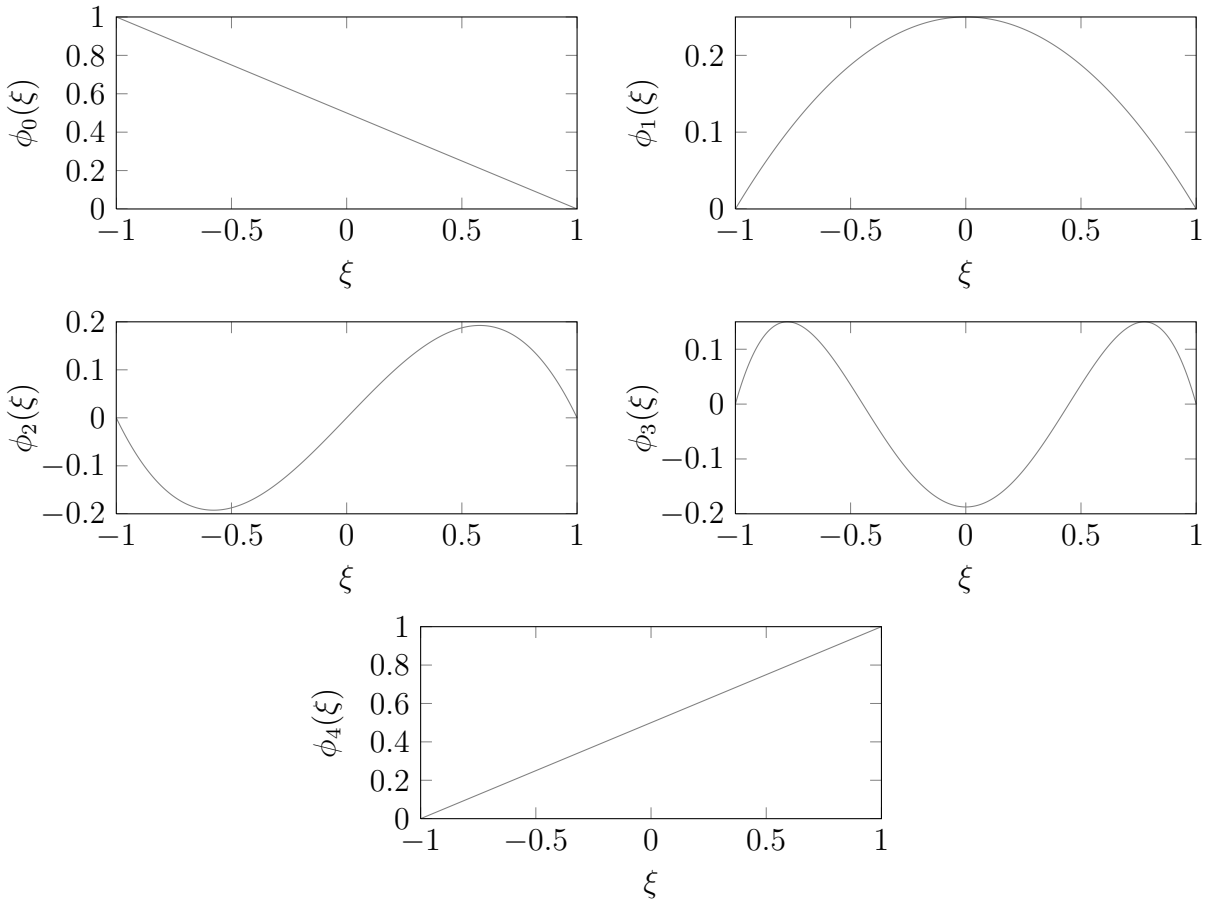

Figure 3.2: Modal basis for one-dimensional element with $P = 4$.

3.3 Discretization in time: high-order splitting

To integrate the equations 3.1-3.3 in time a semi-implicit third-order splitting scheme [19] is employed. The semi-discrete system is given by:

$$\frac{\hat{\mathbf{u}} - \sum_{q=0}^{J} \alpha_q \mathbf{u}^{n-q}}{\Delta t} = -\sum_{q=0}^{J} \beta_q [(\mathbf{u} \cdot \nabla)\mathbf{u}]^{n-q}, \tag{3.8}$$

$$\frac{\hat{\hat{\mathbf{u}}} - \hat{\mathbf{u}}}{\Delta t} = -\nabla p^{n+1}, \tag{3.9}$$

$$\frac{\gamma_0 \mathbf{u}^{n+1} - \hat{\hat{\mathbf{u}}}}{\Delta t} = \frac{1}{Re} \nabla^2 \mathbf{u}^{n+1}, \tag{3.10}$$

Table 3.1: Weights for the stiffly-stable time integrator scheme (see [20], chapter 4.)

Coefficient	1st order ($J = 1$)	2nd order ($J = 2$)	3rd order ($J = 3$)
γ_0	1	3/2	11/6
α_0	1	2	3
α_1	0	-1/2	-3/2
α_2	0	0	1/3
β_0	1	2	3
β_1	0	-1	-3
β_2	0	0	1

The coefficients α_q, β_q and γ_0 are given in table 3.1. Enforcing that $\hat{\mathbf{u}}$ is divergence-free results in the Poisson equation for pressure as follows:

$$\nabla^2 p^{n+1} = \nabla \cdot \left(\frac{\hat{\mathbf{u}}}{\Delta t} \right). \tag{3.11}$$

The pressure-Poisson equation 3.11 is solved with the consistent boundary condition:

$$\frac{\partial p^{n+1}}{\partial n} = -\mathbf{n} \cdot \left[\sum_{q=0}^{J-1} \beta_q [(\mathbf{u} \cdot \nabla)\mathbf{u}]^{n-q} + \frac{1}{Re} \sum_{q=0}^{J-1} \beta_q \nabla \times \omega^{n-q} \right]. \tag{3.12}$$

3.4 Discretization in parametric space: stochastic collocation

3.4.1 Long-time integration limitation

In this section, we intend to discretize dependent variables such as $\theta(\mathbf{x}, t; \boldsymbol{\xi})$ in the parametric space. Note that $\theta(\mathbf{x}, t; \boldsymbol{\xi})$ can be seen as a random process for a fixed $\mathbf{x} := \mathbf{x}_0$. The limitation of polynomial chaos approach in long-time integration, however, prohibits the use of this strategy for approximating random processes such as $\theta(\mathbf{x}_0, t; \boldsymbol{\xi})$ [40]. In other words an attempt to approximate $\theta(\mathbf{x}, t; \boldsymbol{\xi})$ as

$$\theta_M(\mathbf{x}, t; \boldsymbol{\xi}) = \sum_{k=0}^{M} \hat{\theta}_k(\mathbf{x}, t) \phi_k(\boldsymbol{\xi})$$

fails to converge for large t's.

On the other hand, from the design point of view, we are often interested in time-averaged quantities. Particularly, in film cooling applications, the time-averaged distribution of temperature on the blade surface is of great practical importance. Quantifying the effect of uncertainty of boundary conditions on time-averaged temperature of blade surface is in fact the goal of the current research. In general, other quantities such as friction drag, pressure distribution on the blade surface, energy loss are all time-averaged and the approach that is described here can be similarly applied to study stochastic behavior of these quantities. Note that the time-averaged quantities do not satisfy the steady-state Navier-Stokes/energy equations. They are instead the solution of the time-averaged Navier-Stokes/energy equations [11]. We consider the following decomposition of time-dependent quantities:

$$\begin{aligned}
\mathbf{u}(\mathbf{x}, t; \boldsymbol{\xi}) &= \overline{\mathbf{u}}(\mathbf{x}; \boldsymbol{\xi}) + \mathbf{u}'(\mathbf{x}, t; \boldsymbol{\xi}), \\
p(\mathbf{x}, t; \boldsymbol{\xi}) &= \overline{p}(\mathbf{x}; \boldsymbol{\xi}) + p'(\mathbf{x}, t; \boldsymbol{\xi}), \\
\theta(\mathbf{x}, t; \boldsymbol{\xi}) &= \overline{\theta}(\mathbf{x}; \boldsymbol{\xi}) + \theta'(\mathbf{x}, t; \boldsymbol{\xi}),
\end{aligned}$$

where $\overline{(\ .\ )}$ represents the time-average operator and $(\ .\ )'$ represents the fluctuations. The time-averaged quantities satisfy the following system of partial differential equations:

$$\nabla \cdot \overline{\mathbf{u}} = 0, \tag{3.13}$$

$$(\overline{\mathbf{u}} \cdot \nabla)\overline{\mathbf{u}} = -\nabla \overline{p} + \frac{1}{Re}\nabla^2 \overline{\mathbf{u}} + \nabla \cdot \boldsymbol{\tau}^R, \tag{3.14}$$

$$(\overline{\mathbf{u}} \cdot \nabla)\overline{\theta} = \frac{1}{RePr}\nabla^2 \overline{\theta} - \nabla \cdot \mathbf{q}_t, \tag{3.15}$$

where $\boldsymbol{\tau}^R$ is the Reynolds stress and is given by:

$$\boldsymbol{\tau}^R := -\overline{\mathbf{u}' \otimes \mathbf{u}'}, \tag{3.16}$$

and $\mathbf{q}_t$ is the turbulent heat flux given by:

$$\mathbf{q}_t := \overline{\mathbf{u}'\theta'}. \tag{3.17}$$

It is clear that the quadratic fluctuations given by equation 3.16 couple the time-averaged flow to turbulence which gives rise to *turbulence closure problem*. Attempts to model $\boldsymbol{\tau}^R$ and $\mathbf{q}_t$ fall into the category of Reynolds Averaged Navier Stokes (RANS) equations. However as mentioned in chapter 1, the results obtained from RANS simulations have been shown to be unsatisfactory for film cooling applications. In the remaining of this section, we present the numerical strategy to approximate stochastic time-averaged quantities.

3.4.2 Stochastic collocation

We seek the solution of stochastic time-averaged quantities in the form of an ME-gPC expansion as follows:

$$\overline{\mathbf{u}}_M(\mathbf{x};\boldsymbol{\xi}) = \sum_{e=1}^{Ne}\sum_{k=0}^{M} \hat{\overline{\mathbf{u}}}_k^e(\mathbf{x})\phi_k^e(\boldsymbol{\xi}), \tag{3.18}$$

$$\overline{p}_M(\mathbf{x};\boldsymbol{\xi}) = \sum_{e=1}^{Ne}\sum_{k=0}^{M} \hat{\overline{p}}_k^e(\mathbf{x})\phi_k^e(\boldsymbol{\xi}), \tag{3.19}$$

$$\overline{\theta}_M(\mathbf{x};\boldsymbol{\xi}) = \sum_{e=1}^{Ne}\sum_{k=0}^{M} \hat{\overline{\theta}}_k^e(\mathbf{x})\phi_k^e(\boldsymbol{\xi}), \tag{3.20}$$

The expansion coefficients $\hat{\overline{\mathbf{u}}}_k^e$, $\hat{\overline{p}}_k^e(\mathbf{x})$ and $\hat{\overline{\theta}}_k^e(\boldsymbol{x})$ are obtained by employing Galerkin projection [44]:

$$\hat{\overline{\mathbf{u}}}_k^e(\boldsymbol{x}) = \mathbb{E}[\overline{\mathbf{u}}_M(\mathbf{x};\boldsymbol{\xi})\phi_k^e(\boldsymbol{\xi})]/\mathbb{E}[\phi_k^e(\boldsymbol{\xi})^2], \quad 0 \le k \le M, \quad 1 \le e \le Ne, \tag{3.21}$$

$$\hat{\overline{p}}_k^e(\boldsymbol{x}) = \mathbb{E}[\overline{p}_M(\mathbf{x};\boldsymbol{\xi})\phi_k^e(\boldsymbol{\xi})]/\mathbb{E}[\phi_k^e(\boldsymbol{\xi})^2], \quad 0 \le k \le M, \quad 1 \le e \le Ne, \tag{3.22}$$

$$\hat{\overline{\theta}}_k^e(\boldsymbol{x}) = \mathbb{E}[\overline{\theta}_M(\mathbf{x};\boldsymbol{\xi})\phi_k^e(\boldsymbol{\xi})]/\mathbb{E}[\phi_k^e(\boldsymbol{\xi})^2], \quad 0 \le k \le M, \quad 1 \le e \le Ne. \tag{3.23}$$

Equation 2.34 is used to calculate the global $\mathbb{E}[\ .\ ]$ from local expectation $\mathbb{E}_e[\ .\ ]$. At local level the expectation can be estimated using Gauss-quadrature rule. For a generic

time-averaged quantity $f(\boldsymbol{\xi})$ the quadrature rule can be applied as:

$$\mathbb{E}_e[f(\boldsymbol{\xi})] = \int_{B_e} f(\boldsymbol{\xi})\hat{\mu}_e(\boldsymbol{\xi})d\boldsymbol{\xi} \simeq \sum_{i=0}^{Q} w_{(i)}^e f(\boldsymbol{x}; \boldsymbol{\xi}_{(i)}^e), \tag{3.24}$$

where $\{\boldsymbol{\xi}_{(i)}^e, w_{(i)}^e\}_{i=0}^Q$ are a set of $Q+1$ Gauss-quadrature points and weights in element B_e. Note that assuming a one-dimensional case, the $(Q+1)$-point Gauss quadrature formulae is exact to evaluate $\mathbb{E}_e[f]$ for any polynomial f up to degree $2Q+1$. By using the quadrature rule given by equation 3.24 and equation 2.39, the expansion coefficients for time-averaged quantities given by equation 3.21 can be estimated as:

$$\hat{\overline{\mathbf{u}}}_k^e(\boldsymbol{x}) \simeq \sum_{i=0}^{Q} w_{(i)}^e \mathbf{u}(\boldsymbol{x}; \boldsymbol{\xi}_{(i)}^e)\phi_k^e(\boldsymbol{\xi}_{(i)}^e)/{\gamma_k^e}^2, \quad 0 \leq k \leq M, \quad 1 \leq e \leq Ne, \tag{3.25}$$

$$\hat{\overline{p}}_k^e(\boldsymbol{x}) \simeq \sum_{i=0}^{Q} w_{(i)}^e p(\boldsymbol{x}; \boldsymbol{\xi}_{(i)}^e)\phi_k^e(\boldsymbol{\xi}_{(i)}^e)/{\gamma_k^e}^2, \quad 0 \leq k \leq M, \quad 1 \leq e \leq Ne, \tag{3.26}$$

$$\hat{\overline{\theta}}_k^e(\boldsymbol{x}) \simeq \sum_{i=0}^{Q} w_{(i)}^e \theta(\boldsymbol{x}; \boldsymbol{\xi}_{(i)}^e)\phi_k^e(\boldsymbol{\xi}_{(i)}^e)/{\gamma_k^e}^2, \quad 0 \leq k \leq M, \quad 1 \leq e \leq Ne. \tag{3.27}$$

By replacing equation 3.25-3.27 in the polynomial expansion given by equations 3.18-3.20, a low-dimensional representation of random time-averaged quantities is obtained which can serve as an off-line stochastic surrogate model whose evaluation is inexpensive.

Chapter 4
Uncertainty quantification in jet in crossflow

In this chapter, the effect of random boundary condition on a vertical jet in crossflow (JICF) is investigated. The characteristics of the flow in the vertical JICF has close resemblance to film cooling application. Although the application of vertical JICF is not limited to film cooling. Thrust vectoring of high speed turbojets and VSTOL aircrafts, pollutant dispersal from chimneys and fuel injection in combustion chambers are some of the important applications of vertical JICF. For a comprehensive review of applications of JICF see [24].

4.1 Problem definition

The problem setup considered here is identical to that of Ilak *et al.* [17] with the difference of considering a random boundary condition for the jet velocity in the current study. The same problem setup was also the subject of several other studies by Bagheri *et al.* [7], Rowley *et al.* [34] and Schlatter *et al.* [35]. Figure 4.1 shows the schematic of the numerical domain in two perpendicular views. The origin of the coordinate system is located at the jet center and x_1, x_2 and x_3 are aligned with streamwise, wall-normal and spanwise directions respectively. As it is shown in figure 4.1(a) the jet is "flushed" into the crossflow. The characteristic length is the displacement thickness of the crossflow boundary layer ($l_{ref} \equiv \delta^*$) and the crossflow velocity is the characteristic velocity ($u_{ref} \equiv U_\infty$). The Reynolds number based on the mentioned characteristic scales is $Re_\infty \equiv U_\infty \delta^*/\nu = 165$ and $\delta^*/D = 1/3$, where D is the jet diameter. The velocity ratio $R \equiv V_{jet}/U_\infty$ is the ratio of *peak* jet velocity to the crossflow velocity [7], and is considered to be a random parameter *i.e.* $\xi \equiv R$. Note that the velocity ratio serves as an important design parameter for vertical JICF applications, particularly in film cooling applications.

The velocity profile at the jet inlet is specified by:

$$u_{jet}(r) = R(1 - r^2)\exp(-(r/0.7)^4), \tag{4.1}$$

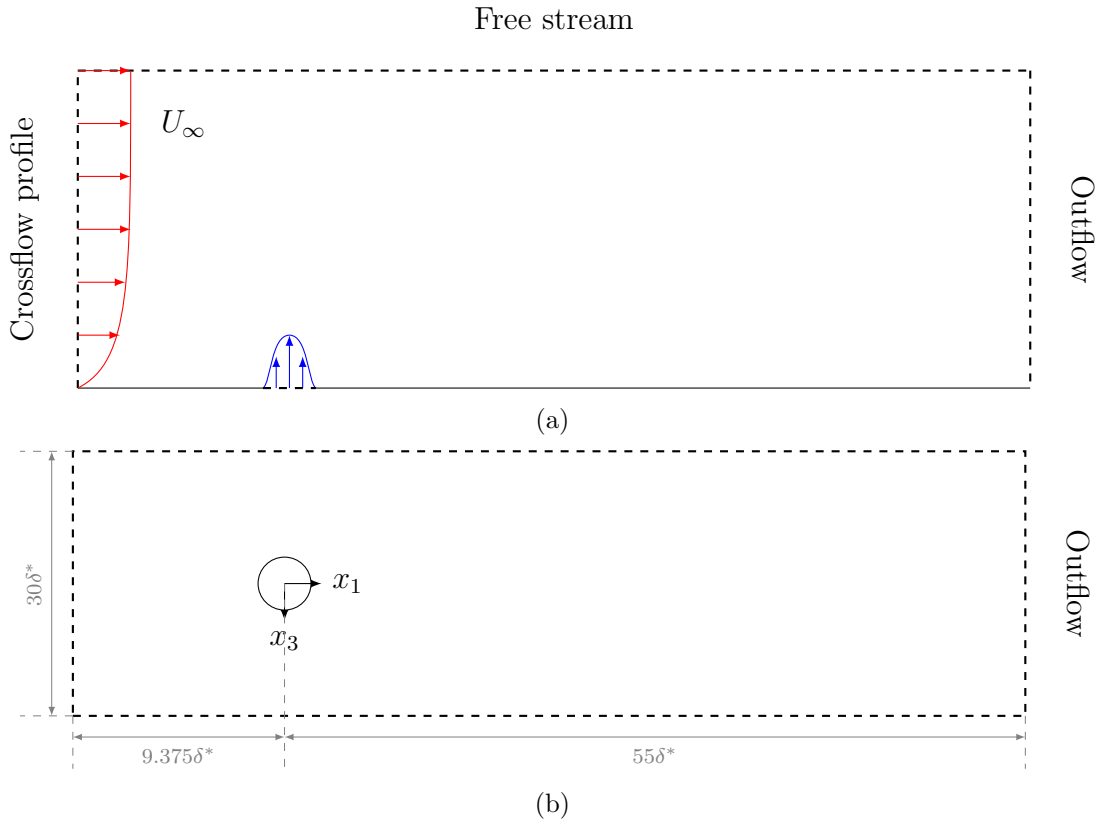

Figure 4.1: The schematic of vertical jet in cross-flow schematic: (a) $x_1 - x_2$ view, (b) $x_1 - x_3$ view.

where r is the normalized distance from the center of the jet:

$$r = 2/D\sqrt{(x_1 - x_{1_j})^2 + (x_3 - x_{3_j})^2},$$

where $(x_{1_j}, x_{3_j}) \equiv (0, 0)$ is the coordinate of jet center in $x_1 - x_3$ plane.

The jet temperature is equal to the coolant temperature *i.e.* $\theta(r) = 0$. At inflow, a laminar boundary layer profile with displacement thickness of $\delta^* \equiv 1$ is specified. The temperature at the inlet is equal to hot gas temperature *i.e.* $\theta = 1$. At the top boundary, free stream condition is used with $\mathbf{u} = (U_\infty, 0, 0)$ and $\theta = 1$. At the outflow boundary, a zero-gradient condition is assumed for both velocity and temperature. At the wall, no-slip boundary condition is used for velocity fields and adiabatic condition is assumed for temperature.

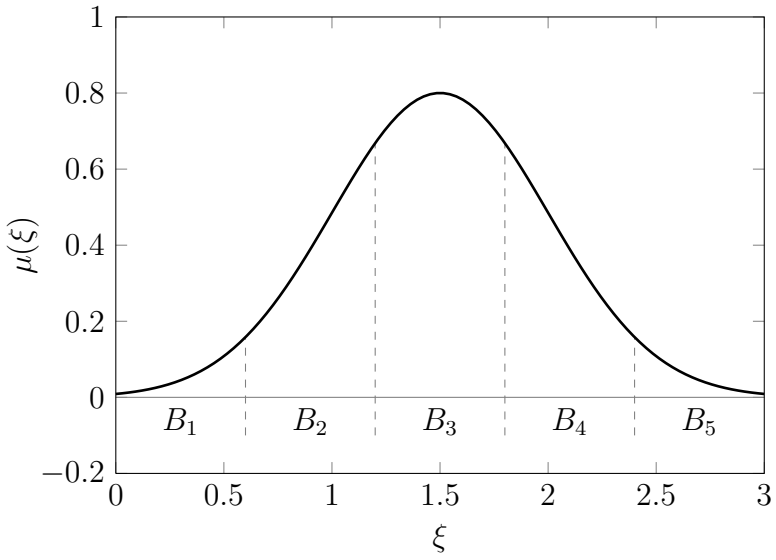

Figure 4.2: Probability density function of velocity ratio; a truncated Gaussian distribution with mean of 1.5 and variance of 0.5. Elemental decomposition ($B_e,\ e = 1, 2, \ldots, 5$) is shown schematically.

In the rest of this thesis we assume that the dimension of the random space is $d = 1$. This assumption is equivalent to assuming that velocity ratio is a random process with the correlation length of $l_c = \infty$. In reality this assumption is valid when the time scales of variations of velocity ratio are much larger that the relevant time scales in the flow. In other words the time variations of velocity ratio occur sufficiently slowly that flow remains statistically steady state at all times.

The random velocity ratio is characterized by symmetrically truncating the tails of a Gaussian distribution around its mean. Considering a Gaussian distribution with the probability density function (PDF) of

$$\rho(\xi) = \frac{1}{\sqrt{2\pi}\sigma} \exp(-(\xi - m)^2)/\sigma^2),$$

with mean of m and the standard deviation of σ, the PDF of the truncated Gaussian

distribution is given by:

$$\mu(\xi) = \begin{cases} \rho(\xi)/\beta, & \mid \xi - m \mid \leq r, \\ 0, & \text{otherwise}, \end{cases} \tag{4.2}$$

Here β is a scaling factor to ensure that $\int_{\mathbb{R}} \mu(\xi) d\xi = 1$. The velocity ratio is assumed to be in the range of $[0,\ 3]$. The mean is $m = 1.5$, and the standard deviation of the Gaussian distribution $\rho(\xi)$ is 0.5 and the standard deviation of $\sigma_R \simeq 0.49$ for the truncated Gaussian distribution $\mu(\xi)$. Figure 4.2 shows the probability density function of the velocity ratio $\mu(\xi)$.

The flow is governed by incompressible Navier-Stokes/energy equations as given by equations 3.1-3.3.

4.2 Statistical information

4.2.1 Film cooling effectiveness

Since adiabatic conditions are used at the surface $x_2 = 0$, the surface temperature field $\theta(\mathbf{x}, t; \xi)$ at $x_2 = 0$ represents a measure of the surface cooling effectiveness by the coolant film, which is defined by:

$$\eta(x_1; \xi) = \frac{1}{w} \int_{-w/2}^{w/2} (1 - \overline{\theta}(\mathbf{x}; \xi)) \mid_{x_2=0} dx_3, \tag{4.3}$$

where $\eta(x_1; \xi)$ is the *spanwise-averaged film cooling effectiveness*, w is the width of the cooled surface. In this study $w = 3D = 9\delta^*$. Variations in velocity ratio (ξ) will lead to variations in temperature and equation 4.3 can be used to quantify this effect on film cooling effectiveness $\eta(x_1; \xi)$.

Further, a *spatially-averaged film cooling effectiveness*, denoted by $\widetilde{\eta}(\xi)$, can be obtained from:

$$\widetilde{\eta}(\xi) = \frac{1}{x_{1_e} - x_{1_s}} \int_{x_{1_s}}^{x_{1_e}} \eta(x_1; \xi) dx_1, \tag{4.4}$$

where x_{1_s} and x_{1_e} denote the beginning and the end of the streamwise interval over which

$\widetilde{\eta}(\xi)$ is calculated. In this study $x_{1_s} = 1.5\delta^*$ and $x_{1_e} = 50\delta^*$.

4.2.2 Friction drag coefficient

The dimensionless *local friction coefficient* that represents normalized wall skin-friction is defined as [27]:

$$c_f(x_1, x_3; \xi) = \frac{\tau_w}{1/2\rho U_\infty^2}, \tag{4.5}$$

where ρ is the fluid density and τ_w is the local shear stress on the wall surface. Since the wall surface is flat, the local shear stress becomes:

$$\tau_w = \frac{2\partial u_1/\partial x_2}{Re},$$

and the *friction drag coefficient*, C_{Df}, is defined as:

$$C_{Df}(\xi) = \frac{\int_{-w/2}^{w/2}\int_{x_{1_s}}^{x_{1_e}} c_f(x_1, x_3; \xi) dx_1 dx_3}{w(x_{1_e} - x_{1_s})} \tag{4.6}$$

4.2.3 Jet trajectory

The jet trajectory is a measure of the penetration of the jet into the crossflow, and it has several definitions. Here we adopt the definition that was introduced by Muppidi [28]. In this definition the jet trajectory is defined by the time-averaged streamline that passes through the center of the jet exit. We denote such a trajectory by $\mathcal{T}_{jet}(x_1; \xi)$.

4.2.4 Statistical moments and sensitivity

The stochastic surrogate model given by equations 3.25-3.27 can now be used to calculate the statistical moments such as expectation using:

$$\mathbb{E}[\overline{\theta}_M(\mathbf{x}; \boldsymbol{\xi})] = \sum_{e=1}^{Ne}\sum_{k=0}^{M} \hat{\overline{\theta}}_k^e(\mathbf{x})\mathbb{E}[\phi_k^e(\boldsymbol{\xi})], \tag{4.7}$$

and by considering the orthogonality of the basis (equation 2.39), the variance is calculated from:

$$\sigma_\theta^2(\mathbf{x}) = \sum_{e=1}^{Ne}\sum_{k=0}^{M} \hat{\overline{\theta}}_k^e(\mathbf{x})^2 \mathbb{E}[\phi_k^e(\boldsymbol{\xi})^2] - \sum_{e=1}^{Ne}\sum_{k=0}^{M} \hat{\overline{\theta}}_k^e(\mathbf{x})^2 \mathbb{E}[\phi_k^e(\boldsymbol{\xi})]^2, \tag{4.8}$$

where $\sigma_\theta(\mathbf{x})$ is the standard deviation of the temperature at point $\mathbf{x}$ in space. The expansion for temperature given by equation 3.20 can accordingly be used to calculate the statistical moments for spanwise-averaged film cooling effectiveness, $\eta(x_1;\boldsymbol{\xi})$, and spatially-averaged film cooling effectiveness, $\widetilde{\eta}(\boldsymbol{\xi})$, by using equations 4.3 and 4.4 respectively.

Another useful statistical information that can be extracted is the *sensitivity* of time-averaged quantities with respect to the random blowing ratio, which, for instance, for temperature is defined as:

$$\mathcal{S}_\theta(\mathbf{x}) = \mathbb{E}\left[\frac{\partial \overline{\theta}_M(\mathbf{x};\boldsymbol{\xi})}{\partial \boldsymbol{\xi}}\right] = \sum_{e=1}^{Ne}\sum_{k=0}^{M} \hat{\overline{\theta}}_k^e(\mathbf{x}) \mathbb{E}[\frac{\partial \phi_k^e(\boldsymbol{\xi})}{\partial \boldsymbol{\xi}}], \tag{4.9}$$

where $\mathcal{S}_\theta(\mathbf{x})$ denotes the sensitivity of time-averaged temperature with respect to variation of the random parameter $\boldsymbol{\xi}$. Since the polynomial basis $\phi_k^e(\boldsymbol{\xi})$ are discontinuous across elements, $\dfrac{\partial \overline{\theta}_M(\mathbf{x};\boldsymbol{\xi})}{\partial \boldsymbol{\xi}}$ is ambiguous. At the common boundary between two elements, we use the average of $\dfrac{\partial \overline{\theta}_M(\mathbf{x};\boldsymbol{\xi})}{\partial \boldsymbol{\xi}}$ from each side, *i.e.*:

$$\frac{\partial \overline{\theta}_M(\mathbf{x};\boldsymbol{\xi})}{\partial \boldsymbol{\xi}} \mid_{\boldsymbol{\xi}=b_e} := 1/2\big(\frac{\partial \overline{\theta}_M(\mathbf{x};\boldsymbol{\xi})}{\partial \boldsymbol{\xi}} \mid_{\boldsymbol{\xi}=b_e^-} + \frac{\partial \overline{\theta}_M(\mathbf{x};\boldsymbol{\xi})}{\partial \boldsymbol{\xi}} \mid_{\boldsymbol{\xi}=b_e^+} \big),$$

where b_e^- resides at the end point of element e and b_e^+ resides at the beginning of element $e+1$. Nevertheless as long as the value of $\dfrac{\partial \overline{\theta}_M(\mathbf{x};\boldsymbol{\xi})}{\partial \boldsymbol{\xi}}$ at boundary points is finite, it does not have any effect on $\mathcal{S}_\theta(\mathbf{x})$, since the boundary points are of measure zero.

Note that using equation 4.3, the expectation, variance and sensitivity for spanwise-

averaged film cooling effectiveness become:

$$\mathbb{E}[\eta(x_1;\boldsymbol{\xi})] = \frac{1}{w}\int_{-w/2}^{w/2}(1-\mathbb{E}[\overline{\theta}_M(\mathbf{x};\boldsymbol{\xi})])\mid_{x_2=0} dx_3, \tag{4.10}$$

$$\sigma^2_\eta(x_1) = \frac{1}{w}\int_{-w/2}^{w/2}\sigma^2_\theta(\mathbf{x})\mid_{x_2=0} dx_3, \tag{4.11}$$

$$\mathcal{S}_\eta(x_1) = \frac{1}{w}\int_{-w/2}^{w/2}\mathcal{S}_\theta(\mathbf{x})\mid_{x_2=0} dx_3. \tag{4.12}$$

4.3 Numerical method

4.3.1 Discretization in physical space

We perform direct numerical simulations for all cases in this study and thus all relevant scales in time and space are resolved. We use spectral/hp element method as described in Section 3.2. A third-order stiffly stable time discretization is used to integrate the equations in time. The details of time discretization are given in Section 3.3.

A three-dimensional view of the computational grid used in this study is shown in figure 4.3(a). Also a close-up and a complete view of the grid are shown in figures 4.3(b) and 4.3(c) respectively. The three-dimensional grid is generated by first generating a quadrilateral grid in $x_1 - x_3$ plane with 844 elements as shown in figure 4.3(c). Near the jet exit, *h-refinement* is performed due to the existence of highest gradients of flow quantities in this region (see figure 4.3(b)). The two-dimensional grid was then swept along the wall-normal direction by creating 26 identical layers as that of shown in figure 4.3(c). In total the grid has 21944 hexahedral elements. The spectral order of $P = 6$ is used which approximately amounts to a total degrees of freedom of 7.5 millions. The same grid as explained here is used throughout this study for all velocity ratios.

4.3.2 Discretization in parametric space

We use ME-gPC as explained in Sections 2.6 and 3.4.2. The parametric space is divided to 5 equidistant elements (*i.e.* $Ne = 5$) as shown in figure 4.2. The details of the decomposition are given in table 4.1. In each element polynomials of order 3 (*i.e.* $M = 3$) that are orthogonal with respect to the local PDF are used as an expansion basis. The

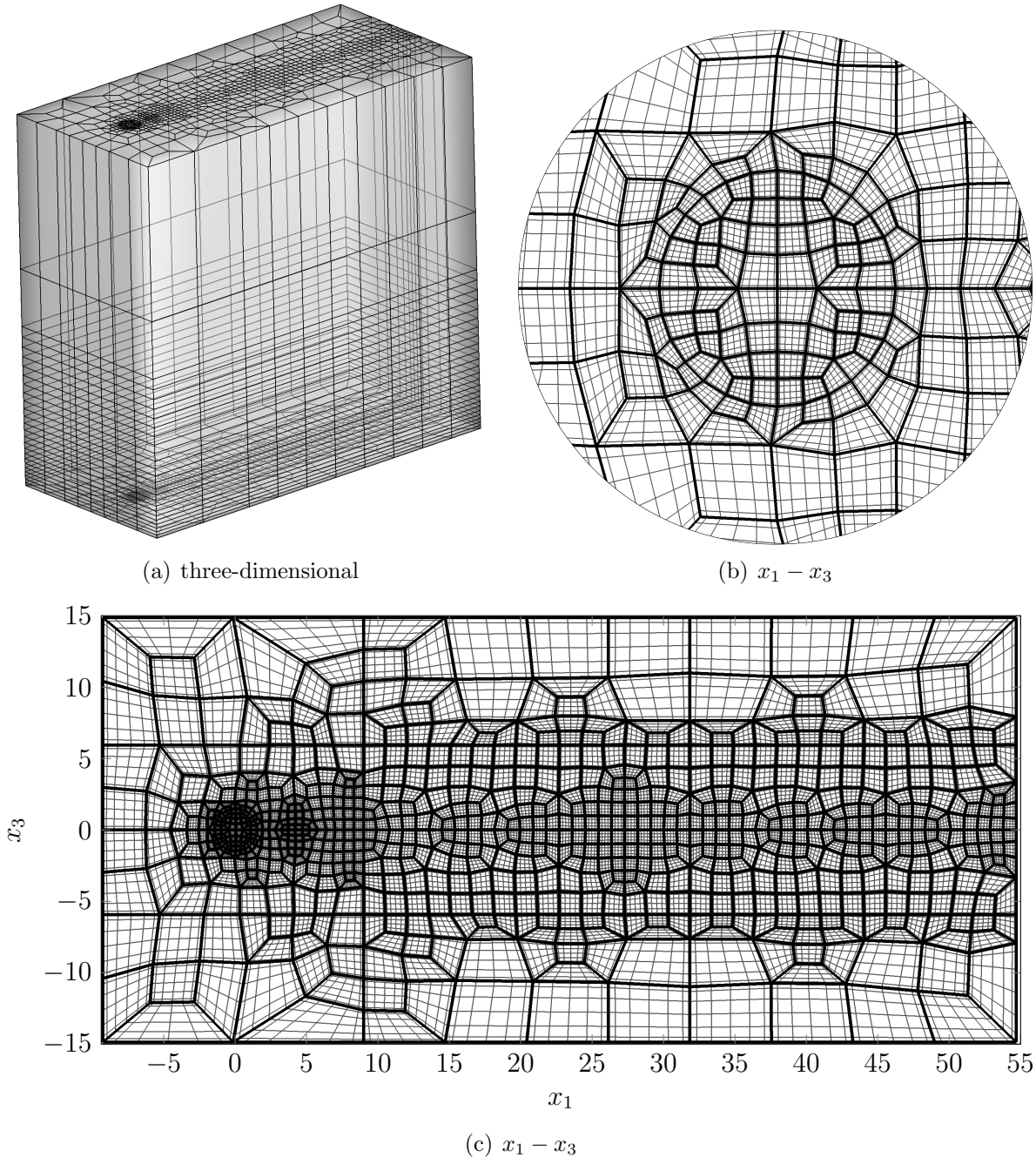

(a) three-dimensional

(b) $x_1 - x_3$

(c) $x_1 - x_3$

Figure 4.3: Hexahedral grid with spectral order $P = 6$ for vertical jet in crossflow. (a) the three dimensional view; (b) a close-up plane ($x_1 - x_3$) view near the jet exit; (c) complete plane ($x_1 - x_3$) view of the grid. The black lines show element boundaries and thin gray lines show Gauss-Lobatto-Legendre quadrature grid.

polynomials are generated numerically using the strategy proposed in [38]. In figure 4.4 the ME-gPC basis used in this study is shown. The basis consists of polynomials up to

Table 4.1: Multi-element decomposition of the random space

Element	a_e	b_e	$Pr(I_{B_e} = 1)$
B_1	0.0	0.6	0.0347
B_2	0.6	1.2	0.2397
B_3	1.2	1.8	0.4527
B_4	1.8	2.4	0.2397
B_5	2.4	3.0	0.0347

degree $M = 3$ within each element. The basis are normalized locally such that

$$\mathbb{E}_e[\phi_i^e(\xi)^2] = 1 \qquad i = 0, 1, \ldots, M \qquad e = 1, 2, \ldots, Ne.$$

The basis consists of polynomials up to degree $M = 3$ within each element. A zero extension of the polynomials outside the element in question is considered. Moreover the polynomials are orthogonal with respect to the local PDF.

4.3.3 Convergence in physical space

In the current study velocity ratio variation belongs to $R \in [0, 3]$. At higher velocity ratios smaller scales are developed, since increasing velocity ratio is equivalent to increasing jet Reynolds number, *i.e.* $Re_j = \overline{U_j} D/\nu$ where $\overline{U_j}$ is the jet average velocity. Therefore grid study is only performed for the highest velocity ratio. Since the same grid is used for all simulations, achieving a grid-independent solution at highest velocity ratio ensures that solution at lower velocity ratios are also grid-independent.

The highest velocity ratio in this study is $R \equiv 2.941$, which is the last quadrature point in the last element ($e = 5$). Since flow at this velocity ratio is turbulent and thus chaotic, only the comparison of time-averaged quantities is meaningful. We perform two direct numerical simulations with spectral order of $P = 5$ and $P = 6$ for the same grid as shown in figure 4.3, thus only *p-refinement* is considered as a grid-refinement strategy. The two simulations were run for $300\delta^*/U_\infty$ non-dimensional time units to allow the initial

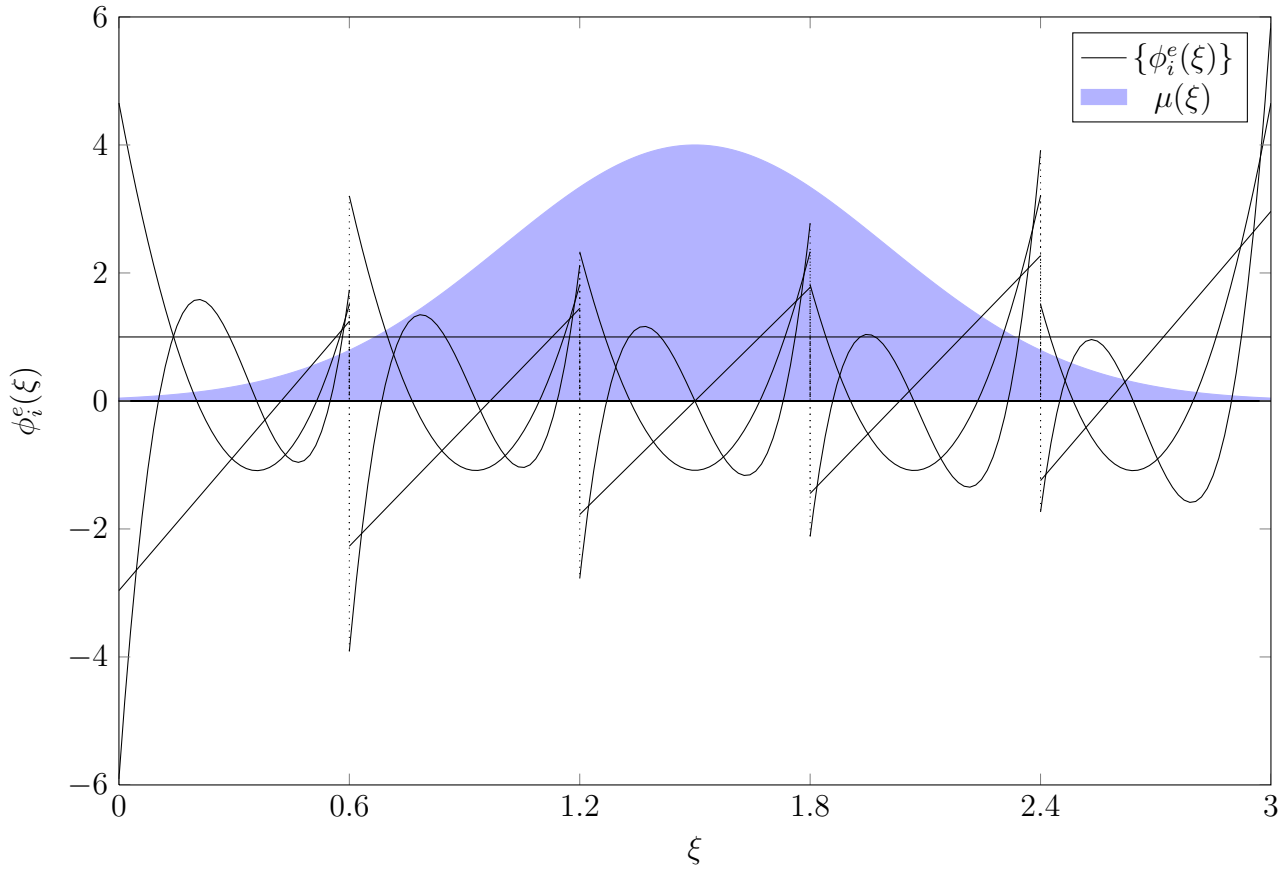

Figure 4.4: The basis of Multi-Element-general-Polynomial-Chaos for the random velocity ratio $R \in [0, 3]$.

transients to exit the domain. The statistics were then collected for another $300\delta^*/U_\infty$ units.

The comparisons of the time-averaged quantities between two grids are shown in figure 4.5. All comparisons are performed in the mid-plane ($x_3 = 0$). Figure 4.5(a) shows the comparison of wall-normal velocity $\overline{u_2}$ at one diameter above the jet exit, *i.e.* $x_2/\delta^* = 3$. Figure 4.5(b) and 4.5(c) show the comparison of streamwise velocity $\overline{u_1}$ and temperature $\overline{\theta}$ profiles at two-jet-diameter distance downstream of the jet center *i.e.* $x_1/\delta^* = 6$. In all cases negligible difference between the solution of the two grids is observed. This shows that further grid refinement is not required. Throughout this study, the grid with spectral order $P = 6$ is used.

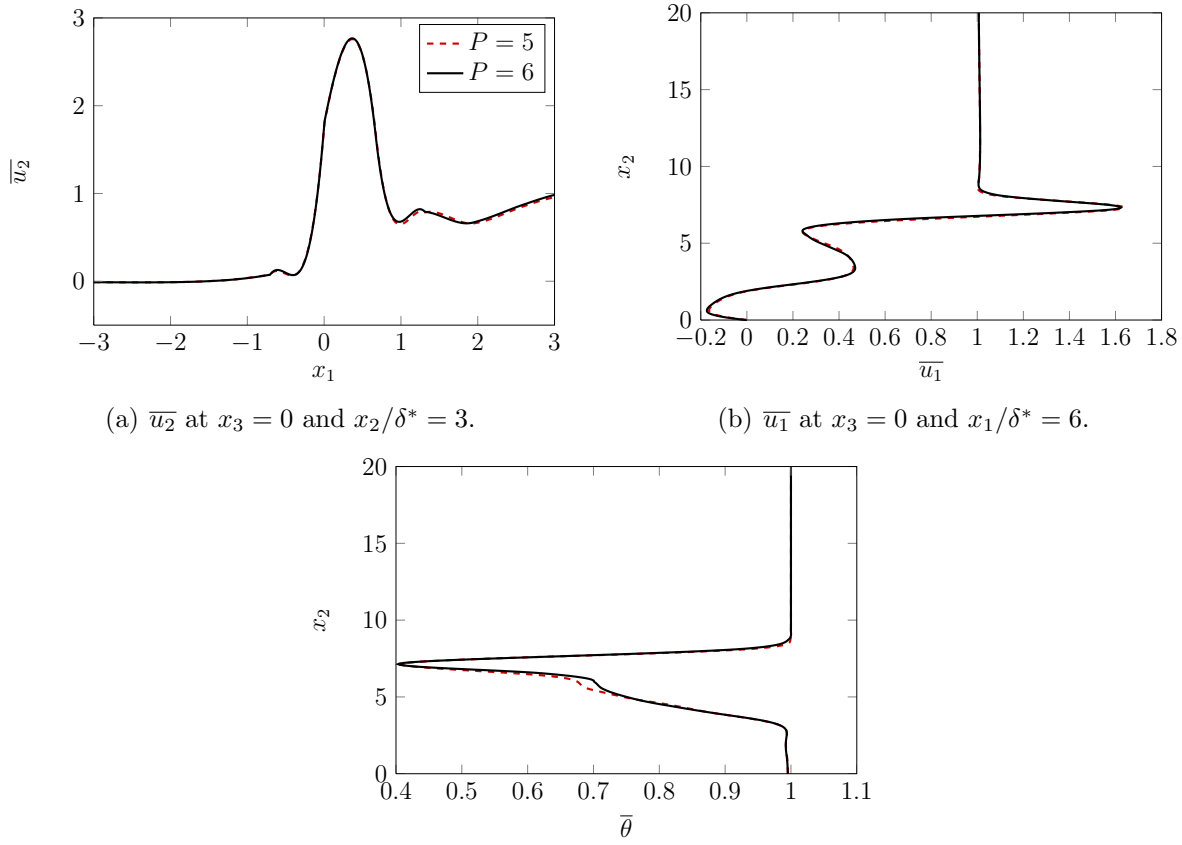

(a) $\overline{u_2}$ at $x_3 = 0$ and $x_2/\delta^* = 3$.

(b) $\overline{u_1}$ at $x_3 = 0$ and $x_1/\delta^* = 6$.

(c) $\overline{\theta}$ at $x_3 = 0$ and $x_1/\delta^* = 6$.

Figure 4.5: Grid study for vertical jet in crossflow with two grids with spectral orders of $P = 5$ and 6 at velocity ratio $R = 2.941$.

4.3.4 Convergence in parametric space

To perform convergence study in the parametric space, we consider spatially-averaged film cooling effectiveness $\widetilde{\eta}(\xi)$ and we compare the *response surface* obtained from different projection orders. In figure 4.6 the response surface obtained from the highest projection order ($M = 3$) is compared with projections with increasing order from $M = 0$ to $M = 2$. The projection order $M = 0$ yields a piecewise constant approximation of $\widetilde{\eta}(\xi)$ as it is shown in figure 4.6(a). As projection order increases to $M = 1$ (piecewise linear), approximation of $\widetilde{\eta}(\xi)$ improves significantly, particularly for $\xi \geq 0.6$ (see figure 4.6(b)). With increasing projection order to $M = 2$, convergence can be observed qualitatively. Note that the ME-gPC basis, as shown in figure 4.4, are hierarchical and thus the rate of decay of Fourier coefficients of the ME-gPC expansion can provide an appropriate measure

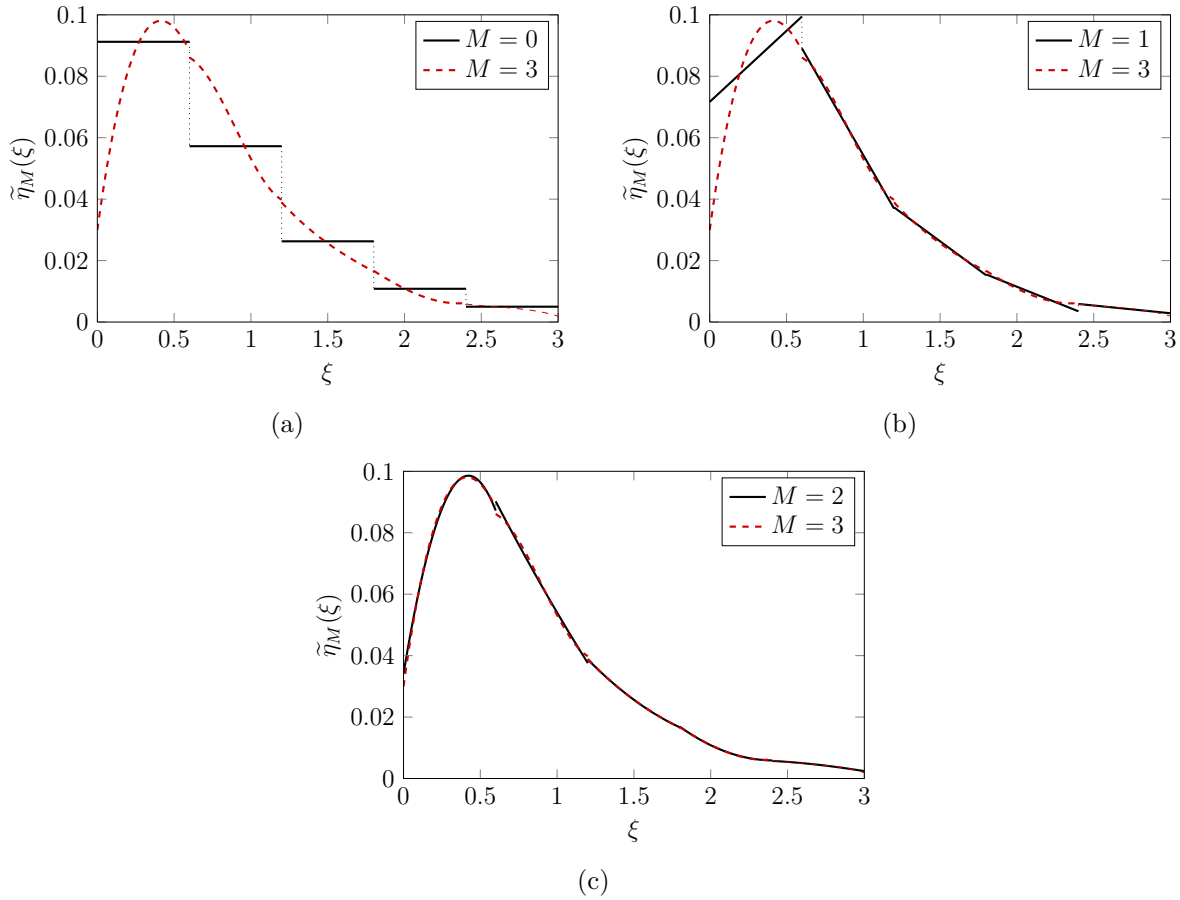

Figure 4.6: Comparisons between finest projection order $M = 3$ and (a) $M = 0$; (b) $M = 1$; (c) $M = 2$.

for the convergence rate. More specifically we consider:

$$\widetilde{\eta}_M(\xi) = \sum_{e=1}^{Ne} \sum_{i=0}^{M} \hat{\eta}_i^e \phi_i^e(\xi), \tag{4.13}$$

where $\widetilde{\eta}_M(\xi)$ is the projection of $\widetilde{\eta}(\xi)$ onto the ME-gPC basis. Since $\{\phi_i^e(\xi)\}$ are also globally orthogonal, and by re-ordering the summations in equation 4.13, we have:

$$\mathbb{E}[\widetilde{\eta}_M(\xi)^2] = \sum_{i=0}^{M} \sum_{e=1}^{Ne} \left(\hat{\eta}_i^e\right)^2 \mathbb{E}[\phi_i^e(\xi)^2].$$

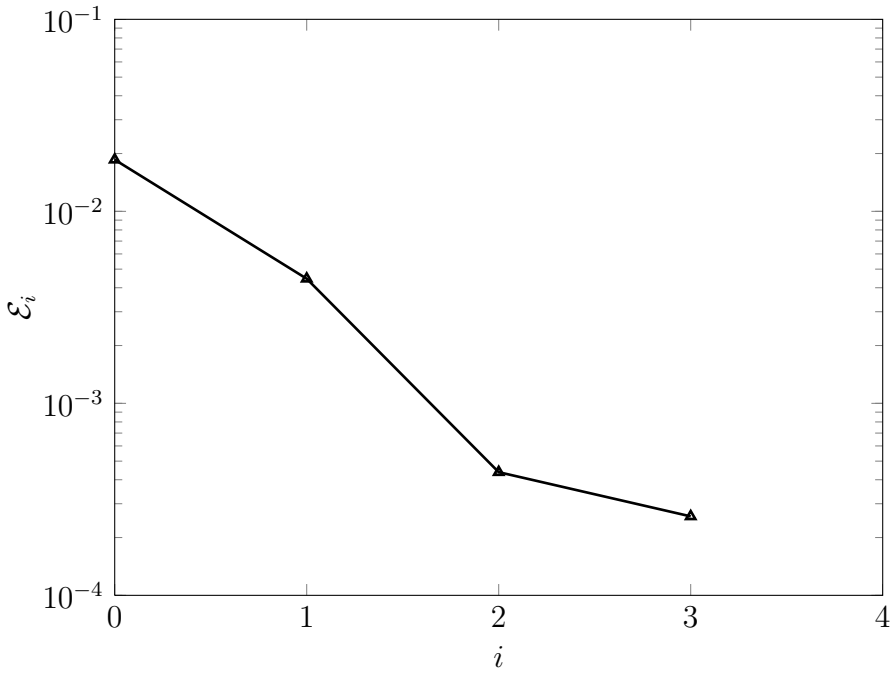

Figure 4.7: Fourier coefficients of ME-gPC expansion for spatially-averaged film cooling effectiveness.

In the above equation $\left(\mathbb{E}[\phi_i^e(\xi)^2]\right)^{1/2}$ is the normalizing factor for $\phi_i^e(\xi)$. Therefore the contribution from increasing projection order by one is:

$$\mathcal{E}_i = \left(\sum_{e=1}^{Ne} \left(\hat{\eta}_i^e\right)^2 \mathbb{E}[\phi_i^e(\xi)^2] \right)^{1/2}, \qquad i = 0, 1, \ldots, M. \tag{4.14}$$

In figure 4.7 Fourier coefficients $\mathcal{E}_i, \quad i = 0, 1, \ldots, M$ for spatially-averaged film cooling effectiveness are shown. Spectral convergence is observed for $0 \leq i \leq 2$. The rate of convergence of Fourier coefficients decrease from $i = 2$ to $i = 3$ and this is attributed to the low-regularity of the response surface due to the several bifurcations occurring in the dynamical system as velocity ratio changes. More details in this regard are given in the next section.

4.4 Bifurcation in dynamical system

In this section we present our observations on the effect of bifurcation occurring in the JICF on the regularity of the various quantities of interest. A physical discussion on the regularity of the response surface in each observation is presented.

Figure 4.11 shows the instantaneous temperature at mid-plane $x_3 = 0$ for all values of R for which direct numerical simulations have been carried out. The values of R, are the quadrature points within each element in the parametric space. The images are arranged such that there are five rows, corresponding to five elements in the parametric space. Each row contains four images corresponding to four quadrature points within each element.

From figure 4.11 it is clear that the jet is steady for velocity ratios $R \leq 0.650$, however at $R = 0.821$ the first bifurcation occurs ($0.650 < R < 0.821$) and a self-sustained oscillation emerges. These oscillations are resulted by periodic shedding of hairpin vortices. These observations are in agreement with the bifurcation analysis carried out by Ilak *et al.* [17]. By increasing velocity ratio, the structure of hairpin vortices becomes more complex. For $R \geq 1.980$ a quasi-periodic behavior emerges which continues up to $R = 2.432$. At $R = 2.561$ a chaotic behavior appears. Further increase in the velocity ratio results in the formation of finer structures. Note that this behavior is to be expected as the velocity ratio is, in fact, proportional to the jet Reynolds number and according to Kolmogorov theory of turbulence, increasing Reynolds number is followed by the appearance of smaller structures.

The effect of bifurcation can be seen in the response surface of film cooling effectiveness. In figure 4.8, spatially-averaged film cooling effectiveness versus velocity ratio is shown. At $R = 0.6$, which is common "edge" between element $e = 1$ and $e = 2$, low-regularity in response surface can be seen. Note that the first bifurcation occurs in the vicinity of $R = 0.675$ which lies in the second element ($e = 2$). For larger velocity ratios ($R > 0.7$) the film cooling effectiveness depicts a relatively smooth behavior despite the fact at least two more bifurcation occurs in the range of $R \in [0.7, 3]$. A physical explanation for this behavior can be given by investigating figures 4.12 and 4.13, which show the time-averaged temperature on the mid-plane ($x_3 = 0$) and on the wall surface ($x_3 = 0$) respectively. Figure 4.12 shows that the jet separates at velocity ratio near $R = 0.568$. The jet separation is responsible for the significant drop in film cooling effectiveness as shown in figure 4.8.

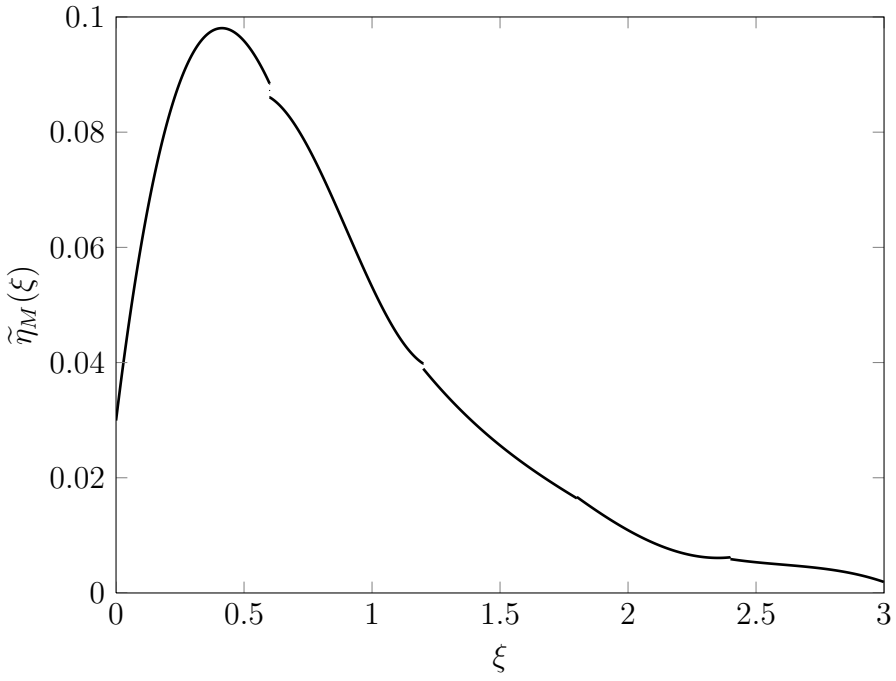

Figure 4.8: Spatially-averaged film cooling effectiveness versus velocity ratio. The projection order is $M = 3$.

The jet body continues to move away from the wall surface as velocity ratio increases, and the film cooling effectiveness decreases correspondingly. As it can be seen in figure 4.13, increasing velocity ratio beyond $R = 2$ has negligible impact on wall temperature. Bagheri [6] and Ilak *et al.* [17] showed that the other two bifurcations occur at $R \simeq 2.25$ and $R \simeq 2.5$. In both of these bifurcation points, the jet has completely separated and the near-wall behavior of the velocity field has negligible impact on the temperature field, which can explain the smooth behavior of the film cooling effectiveness in the neighborhood of these bifurcation points.

The two bifurcations at $R \simeq 2.25$ and $R \simeq 2.5$ can be more visibly observed, if the friction drag coefficient is investigated. Figure 4.9 shows the projected response surface for friction drag coefficient, C_{Df}. The projection order is $M = 3$. Note that unlike the film cooling effectiveness, C_{Df} is strongly dependent on the near-wall dynamics even when the jet has completely separated. As presented by Bagheri [6], the bifurcation that occurs at $R \simeq 2.25$ has the strongest effect on the jet body and the instability modes have low

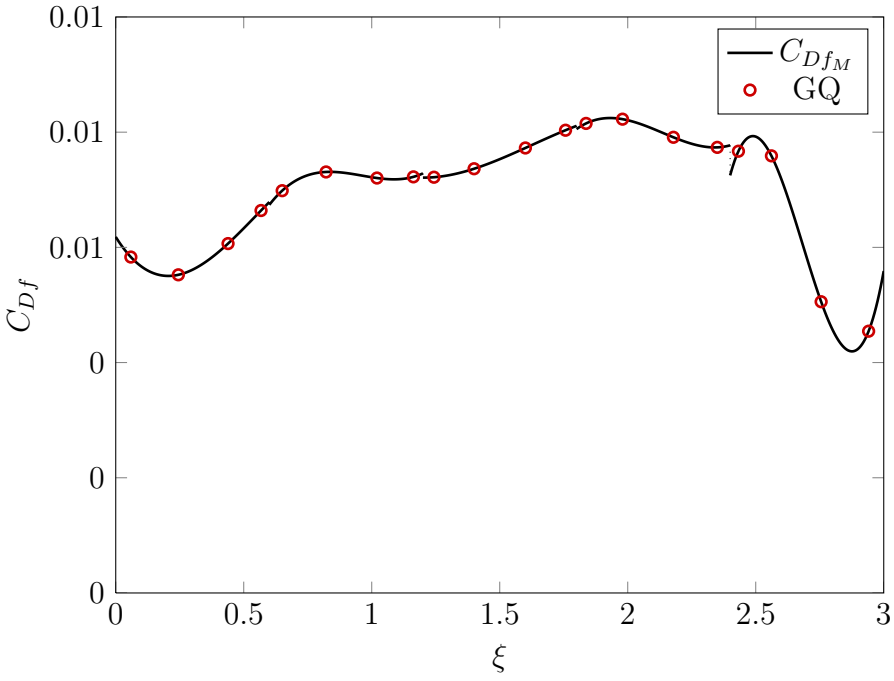

Figure 4.9: Friction drag coefficient versus velocity ratio. The projection order is $M = 3$. GQ: Gauss Quadrature points.

energy in the near-wall region. However the bifurcation that occurs at $R \simeq 2.5$ is a result of von-Kármán instability; an analogy to the instability mechanisms of flow over cylinder. In this analogy, at large enough velocity ratios, the jet serves as a "soft body" to which the crossflow cannot penetrate. As a result the crossflow wraps around the jet body and separates behind it. The separation of the crossflow results in a vortex shedding similar to *von-Kármán vortex street* in flow behind a cylinder. This instability has strong impact on the near-wall flow dynamics. As it is clear from figure 4.9, the drag friction coefficient shows an abrupt change near $R \simeq 2.5$. In fact the polynomial expansion in the last element ($e = 5$) shows numerical oscillations. These oscillations are similar to oscillations observed near discontinuity, which is referred to as *Stochastic Gibbs Phenomenon* [43]. However more refinement is required to identify the nature of "irregularity" and its location.

Figure 4.10 shows the jet trajectory at five streamwise locations versus velocity ratio. At closer distance to the jet center ($x_1 = 5$ and $x_1 = 10$), the trajectory is relatively a smooth function of velocity ratio. However at farther streamwise locations, $\mathcal{T}_{jet}(x_1; \xi)$

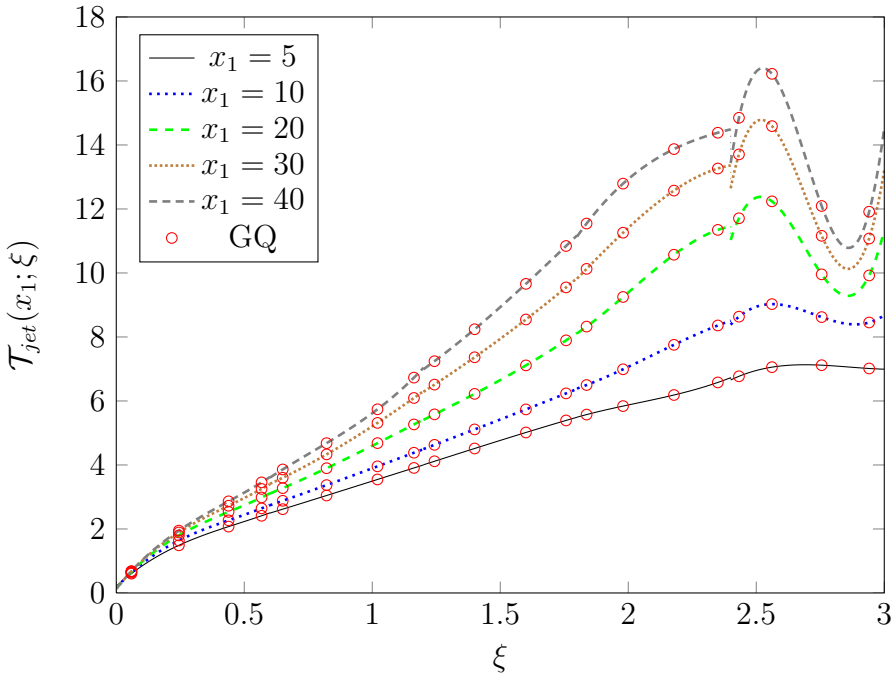

Figure 4.10: Jet trajectory versus velocity ratio at different streamwise locations. The projection order is $M = 3$. GQ: Gauss Quadrature points.

shows oscillations within the fifth element. This indicates that the bifurcation occurring at $R \simeq 2.5$ has significant impact on the jet body as well. In fact as it can be seen from figure 4.11, at $R \geq 2.561$ smaller scales appear in the flow which correspond to a higher amount of turbulence. Since turbulence tends to have a dissipative nature on the time-averaged flow, it reduces the jet penetration.

From the above observations, it can be concluded that the bifurcations of the JICF, result in the presence of low-regularity in the time-averaged quantities. However the regularity of the target function varies with location. Also temperature and velocity field can have different behaviors with respect to the bifurcation parameter. The above argument is by no means a mathematical one; it is mostly inspired from physical intuition confirmed by numerical observations.

4.5 Statistical moments

As explained in Section 4.2.4, once the ME-gPC expansions of time-averaged quantities are constructed, different statistical moments can be computed at very low computational cost. In fact the ME-gPC expansion serves as a surrogate model whose evaluation can be

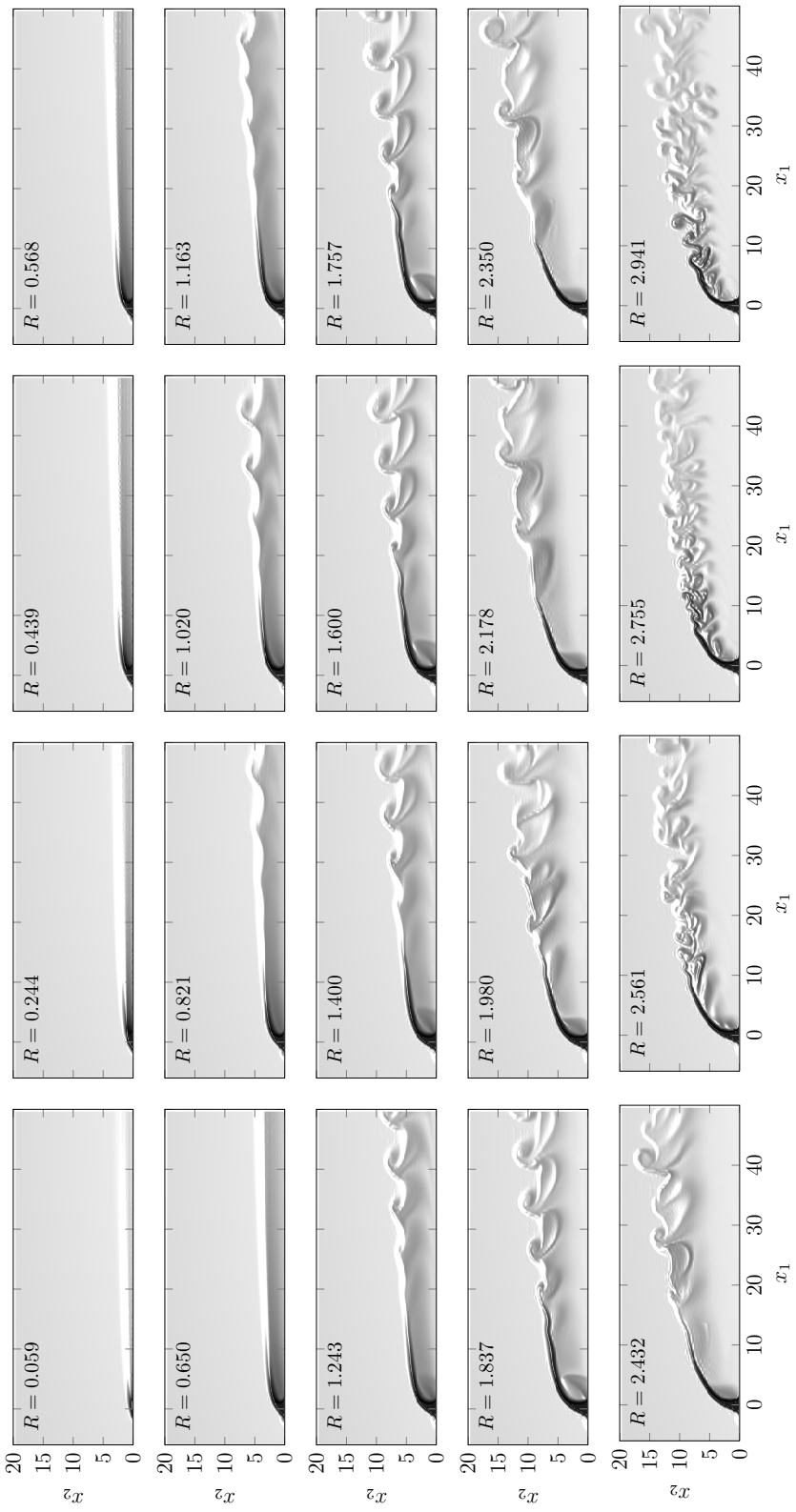

Figure 4.11: Instantaneous temperature surface in the mid-plane ($x_3 = 0$).

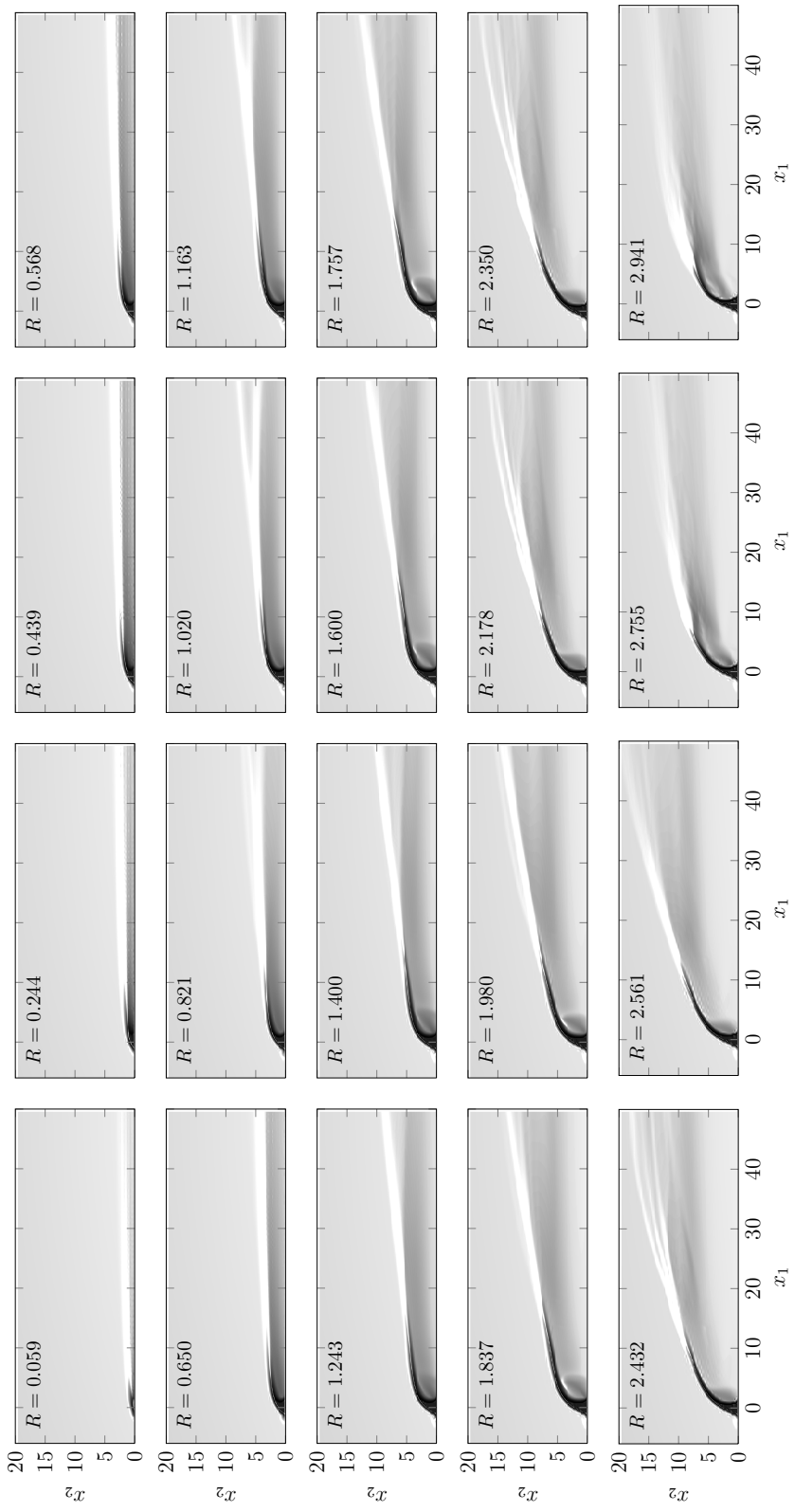

Figure 4.12: Time-averaged temperature surface in the mid-plane ($x_3 = 0$).

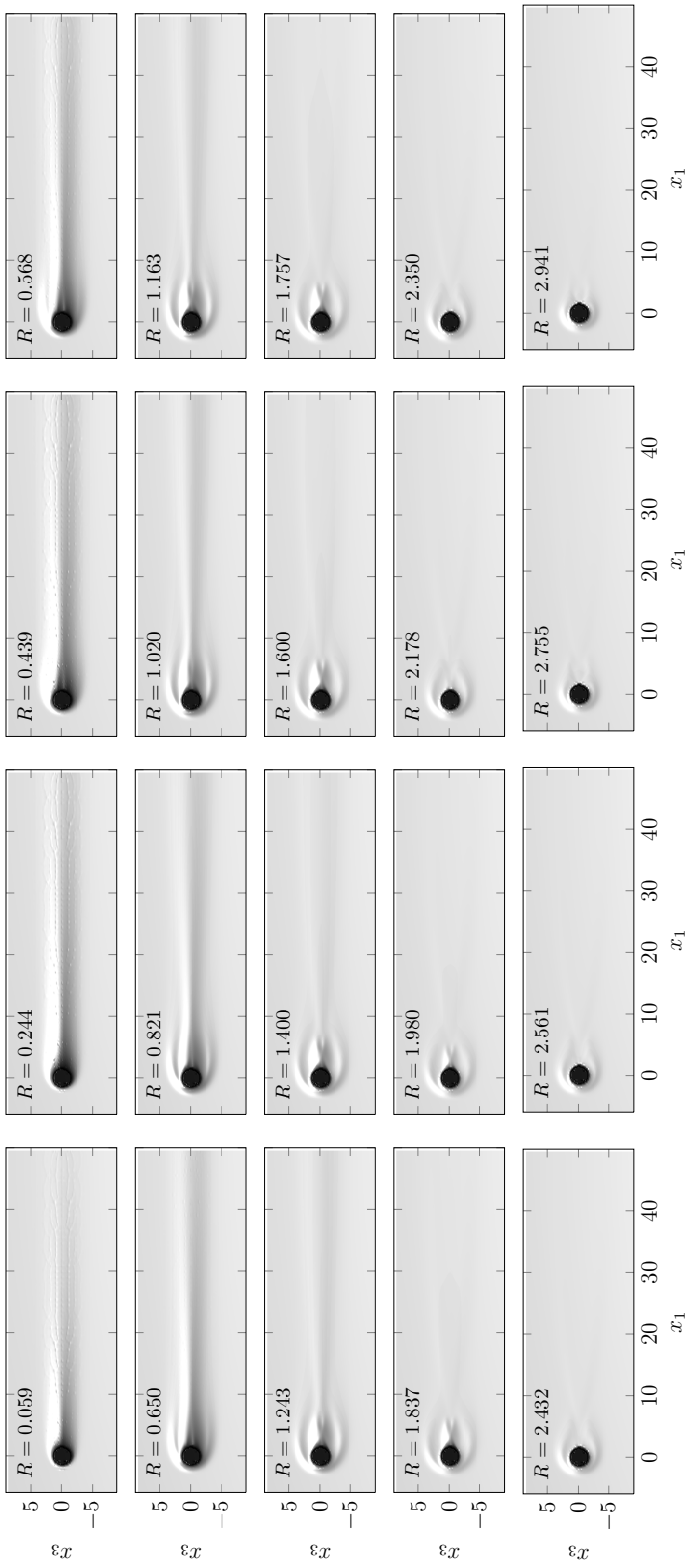

Figure 4.13: Time-averaged temperature on the wall ($x_2 = 0$).

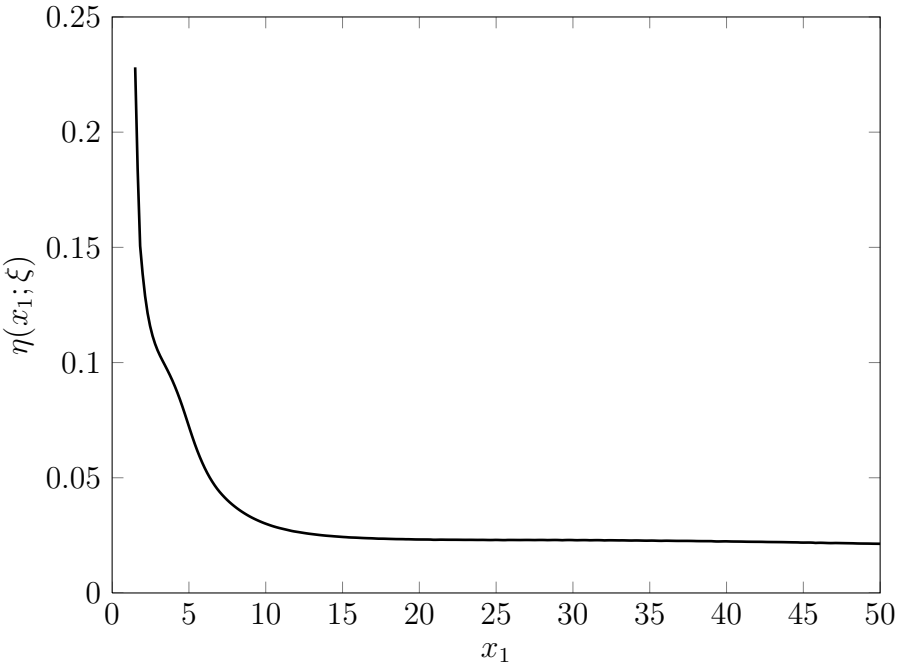

Figure 4.14: Mean spanwise averaged film cooling effectiveness, $\mathbb{E}[\eta(x_1;\xi)]$.

done as offline post-processing.

Figure 4.14 shows the mean of the spanwise-averaged film cooling effectiveness which decays quickly downstream of the jet exit due to mixing that occurs between the coolant and the hot gas. The standard deviation of the spanwise-averaged cooling effectiveness is shown in figure 4.15.

In figure 4.16, the mean jet trajectory along with the jet trajectory associated with velocity ratio that has the maximum likelihood of occurrence, *i.e.* $\xi = 1.5$ are shown.

In figure 4.17 the mean of the jet trajectory along with the standard deviation are shown. The standard deviation grows along the jet trajectory. This observation is in agreement of the nature of the jet shear layer which on average acts as a "noise amplifier". Figure 4.18 shows standard deviation and the sensitivity of the jet trajectory with respect to variation in velocity ratio. Similar to standard deviation, the sensitivity increases along the jet trajectory which is a consequence of the nature of the jet shear layer.

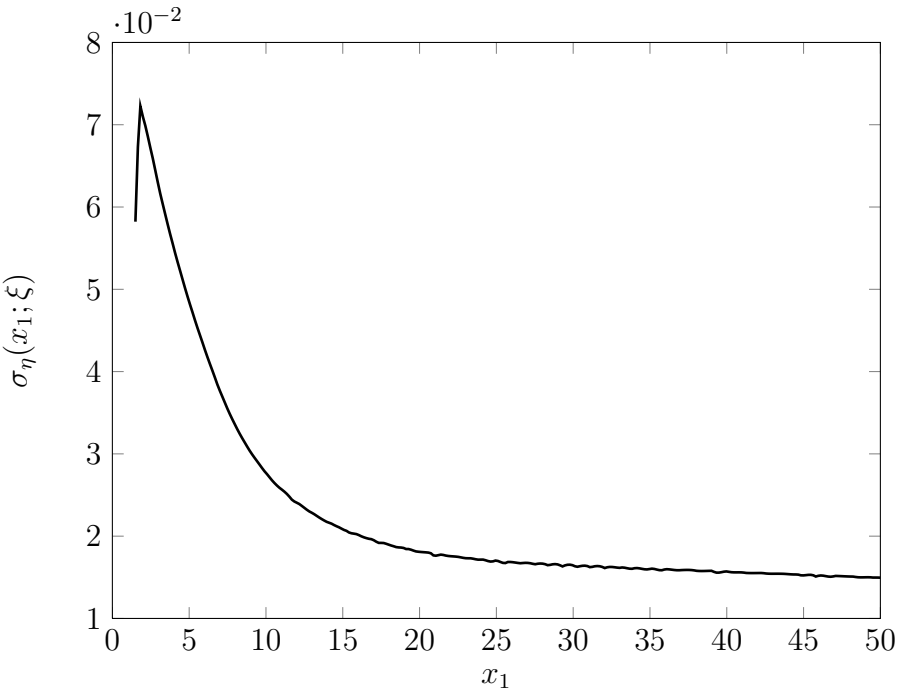

Figure 4.15: Standard deviation of spanwise averaged film cooling effectiveness, $\sigma_\eta(x_1;\xi)$.

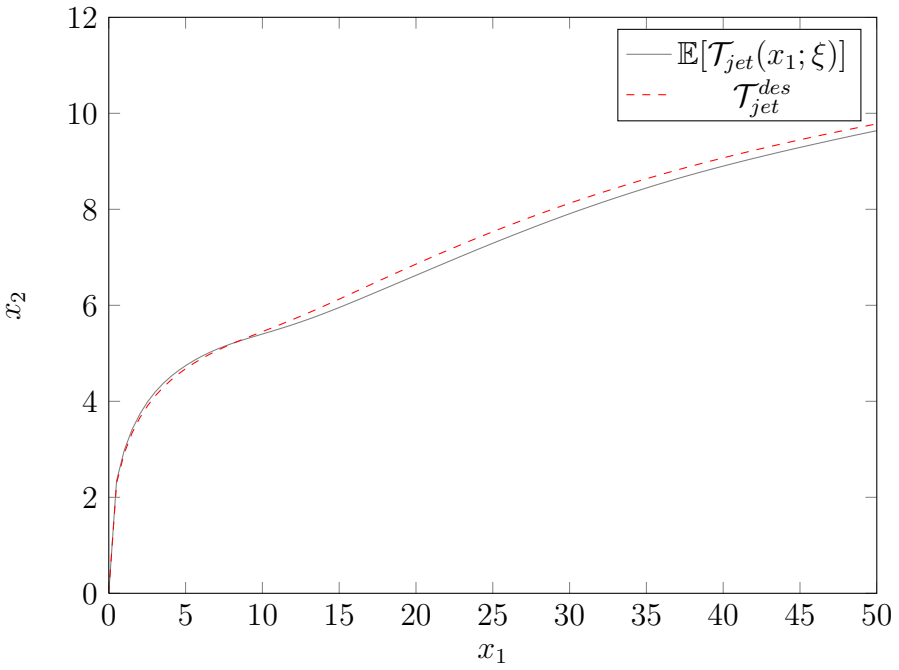

Figure 4.16: Mean jet trajectory $\mathbb{E}[\mathcal{T}_{jet}(x_1;\xi)]$ and the design jet trajectory that corresponds $\mathbb{E}[\mathcal{T}_{jet}(x_1;\xi = 1.5)]$.

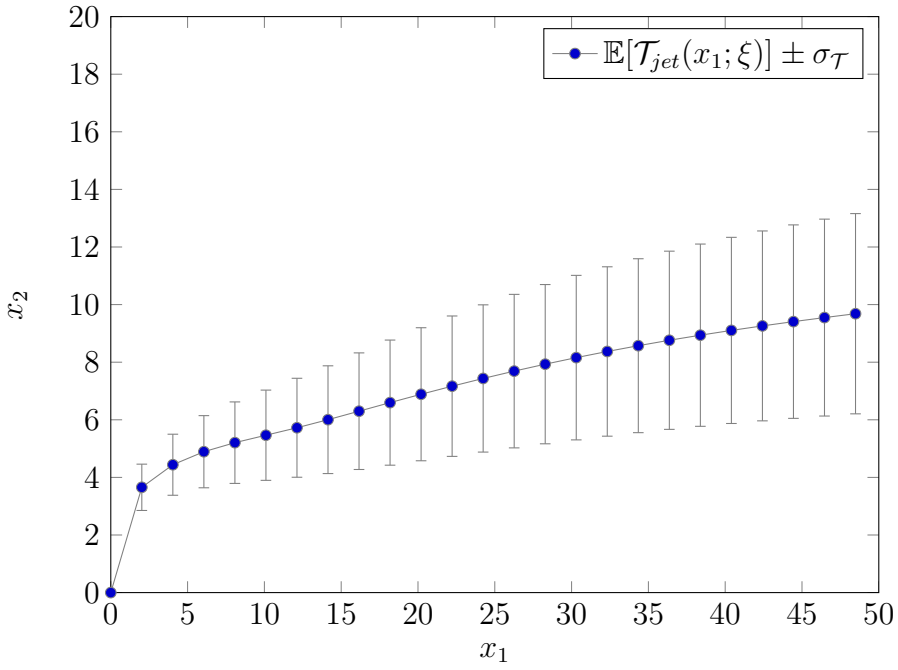

Figure 4.17: Mean jet trajectory $\mathbb{E}[\mathcal{T}_{jet}(x_1;\xi)]$ and the standard deviation.

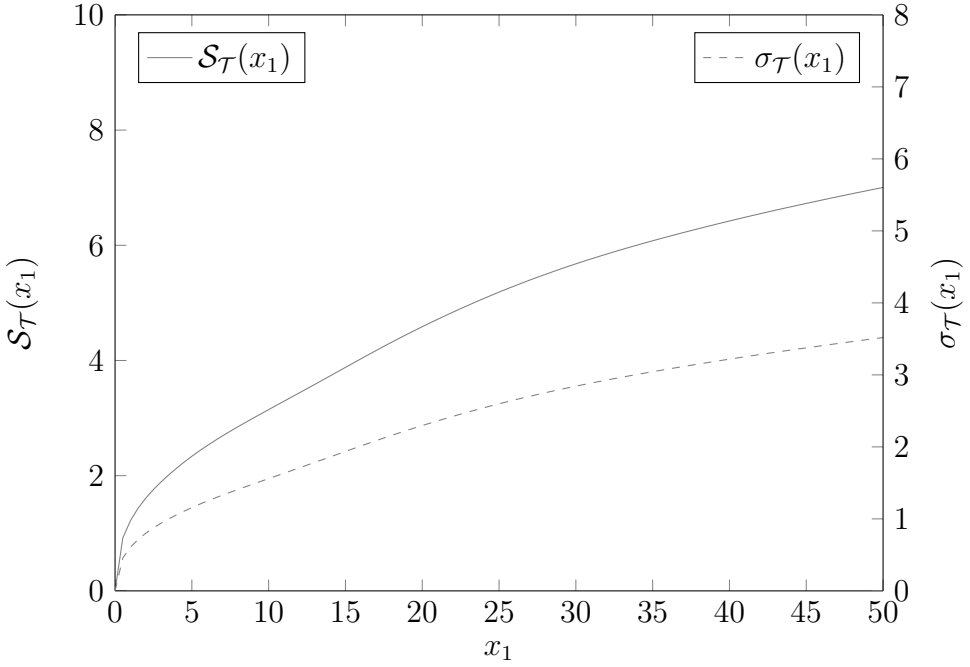

Figure 4.18: Standard deviation and sensitivity of the jet trajectory.

Chapter 5
Summary

In this thesis, the effect of uncertainty of velocity ratio on a vertical jet in a crossflow was investigated using an efficient numerical algorithm. The velocity ratio is a random variable associated with a truncated Gaussian distribution with the mean of 1.5 and the standard deviation of 0.5. The random input is a bifurcation parameter for the dynamical system. A multi-element general polynomial chaos is utilized to discretize the parametric space into non-overlapping elements and an orthogonal polynomial expansion within each element. A pseudo-spectral method has been used to find the expansion coefficients in a non-intrusive manner by sampling the governing equations at Gauss-quadrature points. The spectral element method has been used to perform direct numerical simulation at each quadrature point. The findings of this study can be summarized as:

1. A probabilistic framework to quantify the effect of randomness in the velocity ratio on film cooling effectiveness is presented.

2. The bifurcation of the dynamical system causes low-regularity of the target function.

3. The regularity of the target function varies with location at bifurcation points. Also the regularity of time-averaged temperature is different from that of the velocity field.

4. Multi-element general polynomial chaos is shown to be an effective strategy to investigate the effect of uncertainty of velocity ratio on a jet in a crossflow, particularly due to the presence of several bifurcation points and consequently the low-regularity of the target function.

5. Using the approach in the current study, all the statistical information of the time-averaged quantities, such as probability density function, expectation and variance, sensitivity, etc can be calculated. This information can be integrated into a Bayesian

approach for probabilistic design, and future studies at higher Reynolds number will explore these extensions into probabilistic design.

References

[1] R. S. Abhari. Impact of rotor–stator interaction on turbine blade film cooling. *Journal of Turbomachinery*, 118(1):123–133, 1996.

[2] S. Acharya and M. Tyagi. Large eddy simulation of film cooling flow from an inclined cylindrical jet. *ASME Conference Proceedings*, 2003(36886):517–526, 2003.

[3] S. Acharya, M. Tyagi, and A. Hoda. Flow and heat transfer predictions for film cooling. *Annals of the New York Academy of Sciences*, 934(1):110–125, 2006.

[4] H. Babaee. *Analysis and optimization of film cooling effectiveness*. PhD thesis, Louisiana State University, August 2013.

[5] H. Babaee, S. Acharya, and X. Wan. Optimization of forcing parameters of film cooling effectiveness. In *ASME Conference Proceedings*. ASME, 2013.

[6] S. Bagheri. *Analysis and control of transitional shear flows using global modes*. PhD thesis, Royal Institute of Technology (KTH), 2010.

[7] S. Bagheri, P. Schlatter, P. J. Schmid, and D. S. Henningson. Global stability of a jet in crossflow. *Journal of Fluid Mechanics*, 624:33–44, 4 2009.

[8] G. Bidan and D. E. Nikitopoulos. On steady and pulsed low-blowing-ratio transverse jets. *Journal of Fluid Mechanics*, 714:393–433, 0 2013.

[9] D. G. Bogard and K. A. Thole. Gas turbine film cooling. *Journal of propulsion and power*, 22(2):249–270, 2006.

[10] R. H. Cameron and W. T. Martin. The orthogonal development of non-linear functionals in series of fourier-hermite functionals. *Annals of Mathematics*, 48(2):pp. 385–392, 1947.

[11] P. A. Davidson. *Turbulence: an introduction for scientists and engineers*. Oxford University Press, USA, 2004.

[12] T. F. Fric and A. Roshko. Vortical structure in the wake of a transverse jet. *Journal of Fluid Mechanics*, 279:1–47, 10 1994.

[13] R. G. Ghanem and P. D. Spanos. *Stochastic finite elements: a spectral approach*. Springer-Verlag, New York, 1991.

[14] X. Guo, W. Schroder, and M. Meinke. Large-eddy simulations of film cooling flows. *Computers & Fluids*, 35(6):587 – 606, 2006.

[15] J.C. Han, S. Dutta, and S. Ekkad. *Gas turbine heat transfer and cooling technology*. Taylor & Francis, 2001.

[16] E. Hopf. A mathematical example displaying features of turbulence. *Communications on Pure and Applied Mathematics*, 1(4):303–322, 1948.

[17] M. Ilak, P. Schlatter, S. Bagheri, and D. S. Henningson. Bifurcation and stability analysis of a jet in cross-flow: onset of global instability at a low velocity ratio. *Journal of Fluid Mechanics*, 696:94–121, 2012.

[18] I. V. Iourokina and S. K. Lele. Towards large eddy simulation of film-cooling flows on a model turbine blade leading edge. *AIAA Paper*, 670, 2005.

[19] G. E. Karniadakis, M. Israeli, and S. A. Orszag. High-order splitting methods for the incompressible Navier-Stokes equations. *Journal of Computational Physics*, 97(2):414 – 443, 1991.

[20] G. E. Karniadakis and S. J. Sherwin. *Spectral/hp element methods for computational fluid dynamics*. Oxford University Press, USA, 2005.

[21] R. M. Kelso, T. T. Lim, and A. E. Perry. An experimental study of round jets in cross-flow. *Journal of Fluid Mechanics*, 306:111–144, 0 1996.

[22] H. H. Kuo. *Introduction to stochastic integration*. Springer Verlag, 2006.

[23] L. D. Landau and E. M. Lifshitz. *Fluid Mechanics, Second Edition: Volume 6 (Course of Theoretical Physics)*. Course of theoretical physics / by L. D. Landau and E. M. Lifshitz, Vol. 6. Butterworth-Heinemann, 2 edition, January 1987.

[24] K. Mahesh. The interaction of jets with crossflow. *Annual Review of Fluid Mechanics*, 45(1):379–407, 2013.

[25] F. Muldoon and S. Acharya. DNS study of pulsed film cooling for enhanced cooling effectiveness. *International Journal of Heat and Mass Transfer*, 52(13-14):3118 – 3127, 2009.

[26] F. Muldoon and S. Acharya. Direct numerical simulation of pulsed jets-in-crossflow. *Computers & Fluids*, 39(10):1745 – 1773, 2010.

[27] B. R. Munson, D. F. Young, T. H. Okiishi, and W. W. Huebsch. *Fundamentals of fluid mechanics*, volume 3. Wiley New York, 1998.

[28] S. Muppidi. *Direct numerical simulations and modeling of jets in crossflow*. PhD thesis, University Of Minesota, 2006.

[29] S. Muppidi and K. Mahesh. Direct numerical simulation of round turbulent jets in crossflow. *Journal of Fluid Mechanics*, 574(-1):59–84, 2007.

[30] S. A. Orszag and L. R. Bissonnette. Dynamical properties of truncated wiener-hermite expansions. *Physics of Fluids*, 10(12):2603–2613, 1967.

[31] R. Paley and N. Wiener. *Fourier transforms in the complex domain*. American Mathematical Society, 1934. Includes bibliography.

[32] Y. Peet and S. K. Lele. Near field of film cooling jet issued into a flat plate boundary layer: LES study. *ASME Conference Proceedings*, 2008(43147):409–418, 2008.

[33] P. Renze, W. Schroder, and M. Meinke. Large-eddy simulation of film cooling flows at density gradients. *International Journal of Heat and Fluid Flow*, 29(1):18 – 34, 2008.

[34] C. W. Rowley, I. Mezić, S. Bagheri, P. Schlatter, and D. S. Henningson. Spectral analysis of nonlinear flows. *Journal of Fluid Mechanics*, 641:115–127, 2009.

[35] P. Schlatter, S. Bagheri, and D. S. Henningson. Self-sustained global oscillations in a jet in crossflow. *Theoretical and Computational Fluid Dynamics*, 25:129–146, 2011.

[36] S. H. Smith and M. G. Mungal. Mixing, structure and scaling of the jet in crossflow. *Journal of Fluid Mechanics*, 357:83–122, 1998.

[37] D. Venturi, X. Wan, and G. E. Karniadakis. Stochastic low-dimensional modelling of a random laminar wake past a circular cylinder. *Journal of Fluid Mechanics*, 606:339–367, 2008.

[38] X. Wan and G. E. Karniadakis. Multi-element generalized polynomial chaos for arbitrary probability measures. *SIAM Journal on Scientific Computing*, 28(3):901–928, 2006.

[39] X. Wan and G. E. Karniadakis. An adaptive multi-element generalized polynomial chaos method for stochastic differential equations. *Journal of Computational Physics*, 209(2):617–642, 2005.

[40] X. Wan and G. E. Karniadakis. Long-term behavior of polynomial chaos in stochastic flow simulations. *Computer Methods in Applied Mechanics and Engineering*, 195(41–43):5582 – 5596, 2006.

[41] T. Warburton. *1998 Spectral/hp element methods on polymorphic domains*. PhD thesis, Brown, 1998.

[42] N. Wiener. The homogeneous chaos. *American Journal of Mathematics*, 60(4):pp. 897–936, 1938.

[43] D. Xiu. *The Wiener-Askey polynomial chaos*. PhD thesis, Brown University, 2004.

[44] D. Xiu. Efficient collocational approach for parametric uncertainty analysis. *Communications in computational physics*, 2(2):293–309, 2007.

[45] D. Xiu. Fast numerical methods for stochastic computations: a review. *Communications in computational physics*, 5(2-4):242–272, 2009.

[46] D. Xiu and G. E. Karniadakis. The Wiener–Askey polynomial chaos for stochastic differential equations. *SIAM Journal on Scientific Computing*, 24(2):619–644, 2002.

[47] L. L. Yuan, R. L. Street, and J. H. Ferziger. Large-eddy simulations of a round jet in crossflow. *Journal of Fluid Mechanics*, 379:71–104, 1999.

Vita

Hessam Babaee was born in Tehran, Iran. He obtained the B.Sc. degree in Mechanical Engineering from University of Tehran in 2003, and the M.Sc. in Mechanical Engineering from the same university in 2006. He is currently a candidate for the Doctor of Philosophy degree in Mechanical Engineering at Louisiana State University which will be awarded in August 2013. He is also a candidate for M.Sc. in Applied Mathematics at Louisiana State University which will also be awarded in August 2013.